RESEARCH ARTICLE

Key Points:
- Quasi-DC compressions of the dayside magnetosphere are responses to solar wind ram-pressure changes
- The plasma compression in the dayside is greater than the field compression measured by a satellite
- Field compressions, ram-pressure changes, and flow velocities obey large-value power law statistics

Correspondence to:
J. E. Borovsky,
jborovsky@spacescience.org

Compressional perturbations of the dayside magnetosphere during high-speed-stream-driven geomagnetic storms

Joseph E. Borovsky[1,2] and Michael H. Denton[2,3]

[1]Climate and Space Science and Engineering, University of Michigan, Ann Arbor, Michigan, USA, [2]Space Science Institute, Boulder, Colorado, USA, [3]New Mexico Consortium, Los Alamos, New Mexico, USA

Abstract The quasi-DC compressions of the Earth's dayside magnetic field by ram-pressure fluctuations in the solar wind are characterized by using multiple GOES spacecraft in geosynchronous orbit, multiple Los Alamos spacecraft in geosynchronous orbit, global MHD simulations, and ACE and Wind solar wind measurements. Owing to the inward-outward advection of plasma as the dayside magnetic field is compressed, magnetic field compressions experienced by the plasma in the dayside magnetosphere are greater than the magnetic field compressions measured by a spacecraft. Theoretical calculations indicate that the plasma compression can be a factor of 2 higher than the observed magnetic field compression. The solar wind ram-pressure changes causing the quasi-DC magnetospheric compressions are mostly owed to rapid changes in the solar wind number density associated with the crossing of plasma boundaries; an Earth crossing of a plasma boundary produces a sudden change in the dayside magnetic field strength accompanied by a sudden inward or outward motion of the plasma in the dayside magnetosphere. Superposed epoch analysis of high-speed-stream-driven storms was used to explore solar wind compressions and storm time geosynchronous magnetic field compressions, which are of particular interest for the possible contribution to the energization of the outer electron radiation belt. The occurrence distributions of dayside magnetic field compressions, solar wind ram-pressure changes, and dayside radial plasma flow velocities were investigated: all three quantities approximately obey power law statistics for large values. The approximate power law indices for the distributions of magnetic compressions and ram-pressure changes were both -3.

1. Introduction

Changes in the ram pressure of the solar wind result in changes in the amount of compression of the dayside magnetosphere: these are manifested in the magnetosphere as changes in the magnetic field strength and as radial motions. In this report quasi-DC compressions of the magnetosphere at time scales longer than Pc5 ULF periods will be studied. These compressions may be important for the magnetic pumping of the outer electron radiation belt during high-speed-stream-driven storms.

It is well known that there is a connection between the time-integrated amplitude of magnetospheric ULF oscillations and the intensity of the flux of radiation belt electrons in the outer magnetosphere [e.g., *Rostoker et al.*, 1998; *Mathie and Mann*, 2000; *Friedel et al.*, 2002; *Nakamura et al.*, 2002; *Kozyreva et al.*, 2007; *Romanova and Pilipenko*, 2009; *Borovsky and Denton*, 2014]. The amplitudes of ULF fluctuations in the magnetosphere are related to the solar wind velocity [*Singer et al.*, 1977; *Mathie and Mann*, 2001; *Romanova et al.*, 2007; *Kozyreva et al.*, 2007], to the solar wind density [*Menk et al.*, 2003; *Takahashi and Ukhorskiy*, 2008; *Viall et al.*, 2009], and to the interplanetary magnetic field (IMF) B_z [*Romanova et al.*, 2007], and magnetospheric ULF oscillations are observed to be anomalously intense during high-speed-stream-driven storms [*Takahashi and Ukhorskiy*, 2008; *Borovsky and Denton*, 2010a]. The ULF waves are interpreted as cavity modes of the Earth's magnetosphere [*Kivelson and Southwood*, 1985; *Walker*, 1998]. Much of the magnetospheric ULF wave power is believed to be driven by the solar wind (a) via variations in the ram pressure [*Kepko et al.*, 2002; *Eriksson et al.*, 2006; *Motoba et al.*, 2007; *Kessel*, 2008; *Viall et al.*, 2009; *Berube et al.*, 2014], (b) via Kelvin-Helmholtz instabilities [*Mann et al.*, 1999; *Claudepierre et al.*, 2008], or (c) via bow shock or magnetosheath processes [*Eastwood et al.*, 2011; *Hartinger et al.*, 2013; *Regi et al.*, 2014]. Magnetospheric ULF waves can also arise from kinetic instabilities driven by magnetospheric particles [*Hughes et al.*, 1978; *Ozeke and Mann*, 2008].

Here we are interested in characterizing compressional magnetospheric perturbations at frequencies below the cavity modes of the magnetosphere for input to magnetic-pumping calculations for energetic

particles traversing the dayside magnetosphere. Magnetic pumping is an interplay between compression-decompression cycles and pitch angle scattering [*Alfven*, 1950; *Spitzer and Witten*, 1953; *Schluter*, 1957; *Alfven and Falthammar*, 1963], wherein the pitch angle scattering in a magnetosphere acts as a catalyst to enable the compression-decompression cycles to energize magnetospheric particles [*Alfven*, 1959; *Goertz*, 1978; *Borovsky et al.*, 1981; *Mu*, 1993; *Liu and Rostoker*, 1995; *Rostoker et al.*, 1998; *Liu et al.*, 1999; *Dmitriev et al.*, 2001]. Magnetic pumping is most effective when the pitch angle scattering time scales and the compression-decompression time scales are similar [*Berger et al.*, 1958; *Murty and Varma*, 1958; *Borovsky et al.*, 1981; *Borovsky*, 1986]. For radiation belt electrons in the dayside magnetosphere during high-speed-stream-driven geomagnetic storms, pitch angle scattering is believed to be produced by whistler mode chorus outside of the plasmasphere [*Glauert and Horne*, 2005; *Thorne et al.*, 2005; *Shprits et al.*, 2007] and by electromagnetic ion cyclotron waves [*Kovalevskiy*, 1980, 1981; *Jordanova et al.*, 2006; *Thorne et al.*, 2006; *Spasojevic and Fuselier*, 2009] and whistler mode hiss [*Chan and Holzer*, 1976; *Hayakawa et al.*, 1986; *Summers et al.*, 2008] inside the plasmaspheric drainage plume and the plasmasphere. (In the high-mass-density warm plasma cloak [*Chappell et al.*, 2008], which appears throughout the dayside magnetosphere commencing on day 2 of a high-speed-stream-driven storm [*Borovsky et al.*, 2013], other plasma wave modes might become important.) Since pitch angle-scattering time scales for the radiation belt in the dayside magnetosphere are longer than ULF periods [*Borovsky et al.*, 2014], compression-decompression cycles that are longer than ULF periods are more effective at pumping. Transit time scales for radiation belt electrons across the dayside magnetosphere limit the duration of the compressive time scales of interest for pumping. Here 10 min changes in the magnetic field strength in the dayside magnetosphere will be studied; these 10 min changes correspond to ~20 min cycles of compression-decompression.

This report will relate observations of lower than ULF frequency magnetic field compressions in the dayside magnetosphere at geosynchronous orbit to observations of radial plasma motions in the dayside magnetosphere. The ram-pressure fluctuations will be caused dominantly by solar wind density fluctuations rather than solar wind speed fluctuations. It is argued that the observed magnetic field strength fluctuations in the dayside magnetosphere must be related to radial motions of the magnetic flux surface: the magnitudes of those motions are estimated theoretically, and then those estimates are compared with observed cold-plasma radial flow velocities measured at geosynchronous orbit. The influence of the IMF clock angle on the reaction of the Earth's magnetosphere to solar wind ram pressure changes [cf. *Wing and Sibeck*, 1997; *Wang et al.*, 2007; *Li et al.*, 2013] will not be considered. Superposed epoch averaging during high-speed-stream-driven storms will be used.

This report is organized as follows: in section 2, the mathematical relations between changes in the solar wind ram pressure, changes in the dayside magnetic field strength, and radial plasma motions in the dayside magnetosphere are explored; simulations of the reaction of the magnetosphere to the solar wind using the Lyon-Fedder-Mobarry (LFM) global MHD code are utilized. In section 3 storm time observations of the dayside magnetic field, of dayside plasma flows, and of the solar wind are explored. Statistical values of the dayside magnetic field compressions, the solar wind ram-pressure changes, and the dayside-magnetosphere radial flow velocities are examined in section 4. The results are summarized in section 5. Section 6 contains a discussion about the difficulty of characterizing magnetic field compressions and the associated plasma compressions in the nightside magnetosphere.

2. Dayside-Magnetosphere Expectations for Solar Wind Ram-Pressure Fluctuations

In general, the dayside magnetosphere is compressed by the solar wind into a state where the local magnetic field strength is greater than the dipole field value M_E/r^3, where M_E is the dipole moment of the Earth. Note, however, that the dayside field strength in the magnetosphere can be below the dipole field strength (a) during intervals when the Mach number of the solar wind is low (cf. Figure 19 of *Borovsky et al.* [2009]) or (b) when the cross-polar cap current is strong while the ram pressure of the solar wind is weak (cf. Figures 7 and 8 of *Borovsky et al.* [2013]).

A ballpark estimate of the magnetic field strength along the Sun-Earth line in the dayside magnetosphere can be obtained with the use of an "image-dipole" magnetic field model [*Schield*, 1969]: an image dipole is placed
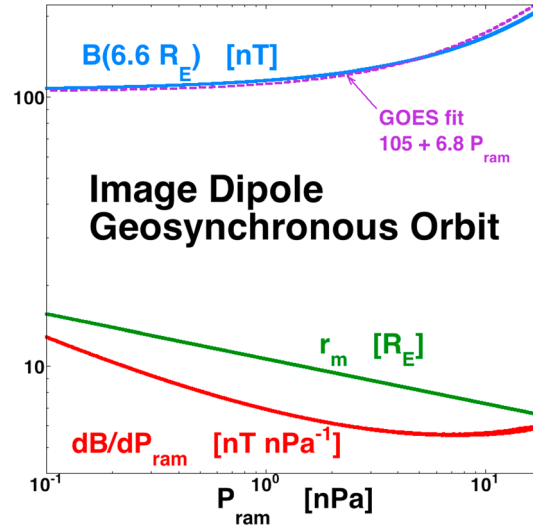
Figure 1. For an image dipole, a number of quantities along the Sun-Earth line are plotted as a function of the solar wind ram pressure.

at a distance of 2 r_m upstream of the Earth, where r_m is the magnetopause standoff distance along the Sun-Earth line. Thus, the field strength is approximated as

$$B(r) = M_E r^{-3} + M_E (2r_m - r)^{-3}, \quad (1)$$

which is valid for $r \leq r_m$. In expression (1) M_E is the Earth's dipole moment, $M_E = 7.8 \times 10^{22}$ Am^2 $= 3.05 \times 10^4$ nT R_E^3 [*Olson and Amit*, 2006]. At the magnetopause ($r = r_m$), the field strength is

$$B_m = B(r_m) = 2M_E r_m^{-3}, \quad (2)$$

which is twice the dipole field strength $M_E r_m^{-3}$. Pressure balance at the magnetopause with the ram pressure P_{ram} of the solar wind $B^2/8\pi = P_{ram}$ yields, with the use of expression (2), the magnetopause standoff distance

$$r_m = \left(M_E^2 / 2\pi P_{ram} \right)^{1/6}. \quad (3)$$

Using expression (3), the magnetopause standoff distance in units of Earth radii (R_E) is plotted as a function of P_{ram} as the green curve in Figure 1. Using expression (3) for r_m in expression (1) yields

$$B(r) = M_E r^{-3} + M_E \left[2\left(M_E^2 / 2\pi P_{ram} \right)^{1/6} - r \right]^{-3} \quad (4)$$

for the magnetic field strength at local noon in the magnetosphere. For geosynchronous orbit ($r = 6.6\ R_E$), expression (4) for the magnetic field strength local noon B_{geo} is plotted as a function of the solar wind ram pressure P_{ram} as the blue solid curve in Figure 1. For comparison the fit to magnetic field strength measurements at geosynchronous orbit local noon during high-speed-stream-driven storms (equation (2) of *Borovsky and Denton* [2010a])

$$B_{geo} = 106 + 6.3\ P_{ram}, \quad (5)$$

where B_{geo} is in nT and P_{ram} is in nPa, is plotted as the purple dashed curve. As can be seen, the data fit of expression (5) (purple) is well described by the image-dipole expression (4) (blue).

The first derivative $\partial B_{geo}/\partial P_{ram}$ of the image-dipole-model magnetic field (expression (4)) at geosynchronous orbit is plotted as a function of P_{ram} as the red curve in Figure 1. The red curve provides an estimate of how much change ΔB_{geo} in the magnetic field strength B_{geo} at geosynchronous orbit noon is expected for a change ΔP_{ram} in the solar wind ram pressure P_{ram}. For typical values of the solar wind ram pressure ($P_{ram} \sim 2$ nPa), the expected change in B_{geo} is about 6 nT for a 1 nPa change in P_{ram}. This is also about the value that would be given by taking the first derivative $\partial B_{geo}/\partial P_{ram}$ of expression (5), which is

$$\partial B_{geo}/\partial P_{ram} = 6.3\ nT/nPa \quad (6)$$

or 6.3 nT for a 1 nPa change in ram pressure. Examples in the literature (e.g., Figure 3a of *Kepko and Spence* [2003], Figure 5a of *Borodkova et al.* [2006], and Figure 5 of *Borodkova et al.* [2008]) yield similar values for changes in the geosynchronous magnetic field strength on the dayside for changes in the solar wind ram pressure.

For the magnetic field strength in the dayside magnetosphere to increase and decrease in response to changes in the solar wind ram pressure, there must be a radial flow of flux inward and outward in the dayside magnetosphere. The image-dipole magnetic field model will provide an estimate of the radial movement of flux and hence an estimate of radial flow velocities in the dayside magnetosphere. This is depicted in Figure 2 for a case where the ram pressure changes from 1 nPa (blue) to 2 nPa (red), and according to expression (3), the magnetopause moves inward from 10.66 R_E (blue) to 9.50 R_E (red). As the magnetic flux moves radially inward and outward, the integral $\int B(r)\ 2\pi r\ d_r$ must be conserved integrated from the surface of the Earth
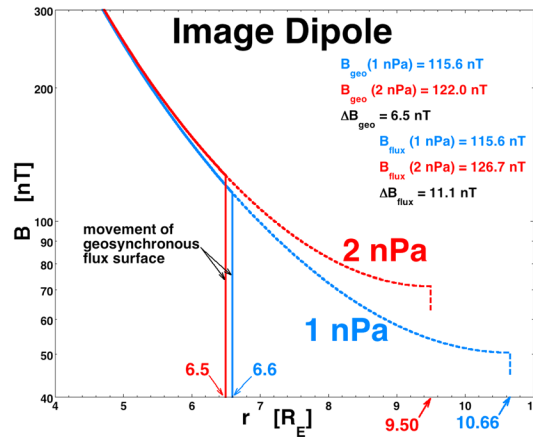
Figure 2. For an image dipole, the magnetic field strength along the Sun-Earth line is plotted for two values of the solar wind ram pressure. The movement of the magnetopause is shown as well as the movement of a flux surface at geosynchronous orbit.

$r = 1$ R_E outward to the radius r_{max} that represents a radially moving flux surface. In Figure 2 the flux surface at geosynchronous orbit when the ram pressure is 1 nPa is drawn as the vertical blue curve at $r = 6.6$ R_E. Integrating $2\pi r$ times the blue curve in Figure 2 from $r = 1$ R_E to $r = 6.6$ R_E yields a value I_o for the integral. Integrating $2\pi r$ times the red curve in Figure 2 from $r = 1$ R_E to a value r_{max} where the integral equals I_o yields a value of $r_{max} = 6.50$ R_E. Thus, the flux surface at geosynchronous orbit moves from $r = 6.6$ R_E to $r = 6.50$ R_E when the ram pressure of the solar wind changes from 1 nPa to 2 nPa.

Using expression (4) in the integral, the displacement of a flux surface at geosynchronous orbit ($r = 6.6$ R_E) is calculated for changes in the solar wind ram pressure by numerically integrating expression (4) before and after the change in P_{ram} and calculating the change in r_{max}. In Figure 3 the change Δr in r_{max} near geosynchronous orbit for a 1 nT change in the geosynchronous magnetic field strength ΔB_{geo} is plotted as a function of the magnetic field strength B_{geo} at geosynchronous orbit. For $B_{geo} = 110$ nT to $B_{geo} = 200$ nT the curve in Figure 3 is well fit by the expression

$$\Delta r / \Delta B_{geo} = -115 \ B_{geo}^{-1.85}, \tag{7}$$

where Δr is in units of R_E and ΔB_{geo} and B_{geo} are both in units of nT. For a ΔB_{geo} that is positive, Δr is negative (earthward). As can be seen, for a wide range in strengths of the dayside field at geosynchronous orbit (110–170 nT) the amount of radial displacement Δr for a change in the field strength ΔB_{geo} is in the range of 0.01 R_E to 0.02 R_E for a 1 nT change in ΔB_{geo}. Thus, the value

$$\Delta r \sim - (0.015 \ R_E / \text{nT}) \Delta B_{geo} \tag{8}$$

can be used as a rule of thumb, with the value being somewhat larger when the field is weaker and the value being somewhat less when the field is stronger.

In the dayside magnetosphere the magnetic flux (and the plasma) moves radially inward and outward as the field strength increases and decreases. The plasma moves radially inward or outward by an $E \times B$ drift because there is an azimuthal induction electric field accompanying $\partial B / \partial t$; it is the local curl (shear) of this induction electric field that also changes the energies of plasma particles to enforce the conservation of their first adiabatic invariants [*Borovsky and Hansen*, 1991]. The radial displacement for a given change in field strength is given by expression (8). The radial velocity of the flow of flux (and plasma) can be obtained by dividing both sides of expression (8) by Δt, the time scale of the magnetic field change in the magnetosphere. With $v_r = \Delta r / \Delta t$ and $\partial B_{geo} / \partial t = \Delta B_{geo} / \Delta t$, this yields

$$v_r \sim - (0.015 \ R_E / \text{nT}) \partial B_{geo} / \partial t = -(95 \ \text{km/nT}) \partial B_{geo} / \partial t \tag{9}$$

for the radial velocity at geosynchronous orbit. Expression (9) yields an expected radial velocity $v_r \sim -95$ km/s $\partial B_{geo} / \partial t$ when $\partial B_{geo} / \partial t$ is measured in units of nT/s or $v_r \sim -1.6$ km/s $\partial B_{geo} / \partial t$ when $\partial B_{geo} / \partial t$ is measured in units of nT/min. Tests of expression (9) using global MHD simulations (this section) and spacecraft measurements (section 3.3) indicate that the image-dipole model underestimates the radial velocity v_r for displacement of the flux surface for a given observed change $\partial B_{geo} / \partial t$ and hence may underestimate the radial displacement Δr of the flux surface for a given change ΔB_{geo}.

Expression (9) can be used to obtain an expression for the geosynchronous orbit radial velocity v_r as a function of the rate of change $\partial P_{ram} / \partial t$ of the solar wind ram pressure by writing $\partial B_{geo} / \partial t$ as $(\partial B_{geo} / \partial P_{ram})(\partial P_{ram} / \partial t)$ in expression (9), which yields

$$v_r = -(95 \ \text{km/nT})(\partial B_{geo} / \partial P_{ram})(\partial P_{ram} / \partial t) = -(599 \ \text{km/nPa}) \partial P_{ram} / \partial t, \tag{10}$$
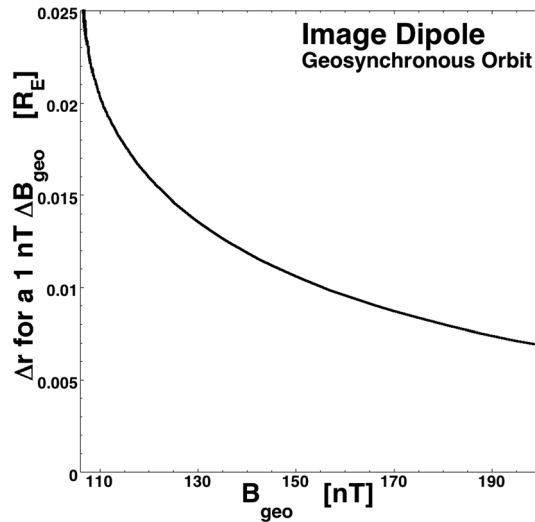
Figure 3. For an image dipole, the radial displacement of a geosynchronous flux surface (in R_E) for a 1 nT change in the field strength at geosynchronous orbit is plotted as a function of the field strength at geosynchronous orbit.
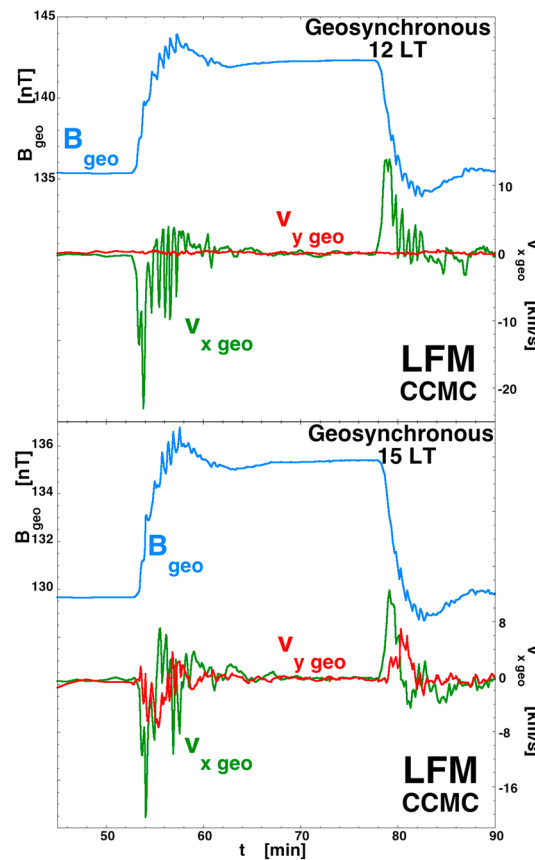

Figure 4. For a solar wind-density increase then decrease, the magnetic field strength at geosynchronous orbit is plotted in blue (left axis) and the v_x and v_y (GSM coordinates) plasma flow velocity components at geosynchronous are plotted in green and red (right axis). The top plot is for local noon, and the bottom plot is for 15:00 LT (CCMC LFM simulation runs Joe_Borovsky_111014_2b and Joe_Borovsky_111014_2b).

where expression (6) was utilized to replace $\partial B_{geo}/\partial P_{ram}$. Here $\partial P_{ram}/\partial t$ is the time rate of change of P_{ram} at the magnetopause. Note that the temporal profiles of rapid changes in the solar wind will be altered by advection through the magnetosheath, which time delays all temporal features by a few minutes [*Borovsky*, 2012a] and has the feature hitting different parts of the magnetopause at different times, effectively broadening the temporal profile.

To demonstrate this radial flow in the dayside magnetosphere (Figure 4), a global MHD simulation of the solar wind-driven magnetosphere is performed with the LFM (CMIT LFM-MIX) simulation code [*Lyon et al.*, 2004; *Merkin and Lyon*, 2010] at the Community Coordinated Modeling Center [*Rastatter et al.*, 2012]. Under purely northward IMF, an increase-then-decrease density step in the solar wind is run past the Earth without changing the solar wind speed (400 km/s). After 55 min of density $n_{sw} = 5\,cm^{-3}$, the solar wind density is suddenly switched to $n_{sw} = 7.5\,cm^{-3}$, and then 20 min later it is switched back to $n_{sw} = 5\,cm^{-3}$. The ram pressure associated with this increase-decrease density step moving at 400 km/s goes from $P_{ram} = 1.34\,nPa$ to $P_{ram} = 2.00\,nPa$ and then back to $P_{ram} = 1.34\,nPa$. In the two plots of Figure 4 the magnetic field strength B_{geo} in the LFM simulation at geosynchronous orbit local noon (top plot) and at geosynchronous orbit 15:00 LT (bottom plot) is plotted (blue, left axis) as a function of time; at the same locations in the LFM simulation the GSM X component of the plasma flow velocity v_{xgeo} (green, right axis) and the GSM Y component of the plasma flow velocity v_{ygeo} (red, right axis) are also plotted as functions of time. As can be seen in the top plot, at about $t = 55$ min the magnetic field strength at geosynchronous orbit local noon rises and this rise in field strength is accompanied by a negative v_{xgeo} (earthward) flow; 20 min later the field strength B_{geo} drops and this drop is accompanied by a positive (sunward)
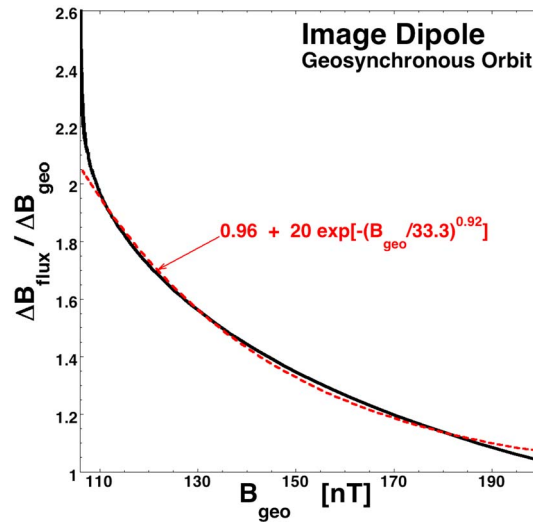
Figure 5. For an image dipole, the ratio of the change in magnetic field strength at a flux surface moving from geosynchronous orbit to the change in magnetic field strength at geosynchronous orbit is plotted as a function of the field strength at geosynchronous orbit.

flow. Note the temporal ringing in the flow velocities with a period of about 40 s; this ringing may be caused by Alfven wave transients in the very low density ($n{\sim}0.07\,\mathrm{cm}^{-3}$) dayside magnetosphere of the simulation (John Lyon, private communication 2015). In this simulation the flow velocities at geosynchronous orbit associated with the change in magnetic field strength are about 20 km/s. In the bottom plot of Figure 4 the earthward then sunward flows are still seen 3 h away from local noon, although less intense. Note that the temporal behavior of the system is not fully resolved in the data output of the LFM simulation, but the radial flow velocities captured in the 1 min resolution output were greater than 20 km/s at geosynchronous orbit.

Expression (9) can be applied to connect the change in the magnetic field strength at geosynchronous orbit to the radial flow velocity in the top plot of Figure 4. During the negative velocity pulse at $t \approx 55$ the magnetic field rate of change is $\partial B_{\mathrm{geo}}/\partial t = 5.5\,\mathrm{nT/min} = 8.7 \times 10^{-2}\,\mathrm{nT/s}$; using this value in expression (9) yields a prediction $v_r = -8.7$ km/s. This predicted velocity is a factor of 2 lower than the observed peak plasma flow velocity in the simulation. During the positive velocity pulse at $t \approx 78$ in the top plot of Figure 4 the magnetic field strength decreases at a rate $\partial B_{\mathrm{geo}}/\partial t = -4.1\,\mathrm{nT/min} = -6.8 \times 10^{-2}\,\mathrm{nT/s}$; using this value in expression (9) yields a prediction $v_r = +6.5$ km/s. This predicted velocity is again about a factor of 2 lower than the observed peak flow velocity. This test may indicate that the image-dipole model (expression (9)) underestimates the radial displacement of the flux surface for a given observed change $\partial B_{\mathrm{geo}}/\partial t$.

As the magnetic field strength at geosynchronous orbit increases and decreases, the flux surface at geosynchronous orbit moves radially inward and outward with a radial displacement given approximately by expression (8). This is shown in Figure 2 for a positive change ΔB_{geo} in the magnetic field strength at geosynchronous orbit. In Figure 2 when the magnetic field strength at geosynchronous orbit increases the plasma that was at geosynchronous orbit moves inward to a new location with a new magnetic field strength, the change in the field strength ΔB_{flux} experienced by the plasma that moves with the flux surface will be larger than the change in the field strength ΔB_{geo} measured by a spacecraft that remains at geosynchronous orbit. By computationally tracking the motion of the flux surface in the image-dipole model, the ratio of magnetic field strength change ΔB_{flux} of plasma moving with the flux surface in the vicinity of geosynchronous orbit to the magnetic field strength change ΔB_{geo} at geosynchronous orbit is calculated and plotted in black as a function of the geosynchronous field strength B_{geo} in Figure 5. For $B_{\mathrm{geo}} = 110$ nT to $B_{\mathrm{geo}} = 200$ nT the curve in Figure 5 is well fit by the stretched exponential function

$$\Delta B_{\mathrm{flux}}/\Delta B_{\mathrm{geo}} = 0.96 + 20\exp\left(-\left[B_{\mathrm{geo}}/33.3\right]^{0.92}\right), \qquad (11)$$

where B_{geo} is in units of nT. Expression (11) is plotted as the red dashed curve in Figure 5. As can be seen, for a mildly compressed dipole ($B_{\mathrm{geo}}{\sim}110$ nT), the field strength change of the plasma is about twice the field strength change at geosynchronous orbit, and for a more strongly compressed dipole ($B_{\mathrm{geo}}{\sim}135$ nT), the field strength change of the plasma is about 1.5 times the field strength change at geosynchronous orbit. Of course the magnetospheric plasma is compressed when the field is compressed [e.g., *Chen*, 1974]: wherever there is a $\partial B/\partial t$, there is a nonzero curl of the electric field which produces an $E \times B$ drift with a nonzero divergence which compresses the plasma. Confirming the prediction of expression (11) by measuring the amount of compression of the plasma in the magnetosphere is in general not possible, since the parcels of plasma move radially as they are compressed. Analysis (not done here) of the evolution of plasma and magnetic field
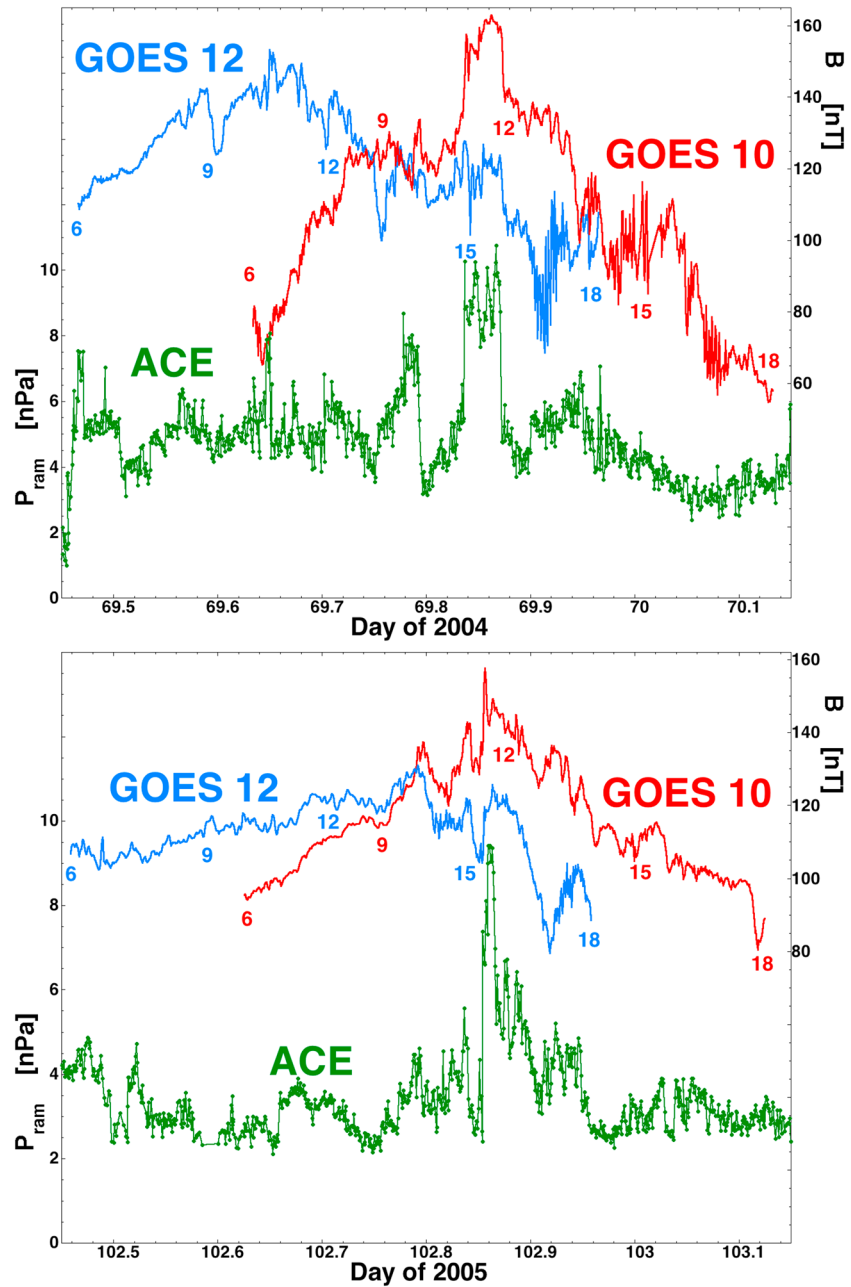
Figure 6. For single crossings of the dayside magnetosphere by GOES 10 (red) and GOES 12 (blue), the magnetic field strength at geosynchronous orbit (right axis) is plotted as a function of time. The ram pressure of the solar wind as measured by ACE is plotted in green (left axis), time shifted to Earth by the solar wind speed. (top) 9–10 March 2004 and (bottom) 12–13 April 2005.

strength with a radial alignment of two or more spacecraft along the Sun-Earth line in the magnetosphere could provide an observed quantification of the amount of plasma compression.

3. Storm Time Observations of Magnetic Compressions, Radial Flow Velocities, and the Solar Wind

3.1. Data Methods

To measure the magnetic field strength at geosynchronous orbit in the dayside magnetosphere, vector magnetic field measurements from the fluxgate magnetometers on the GOES spacecraft [*Dunham et al.*, 1996; *Singer et al.*,
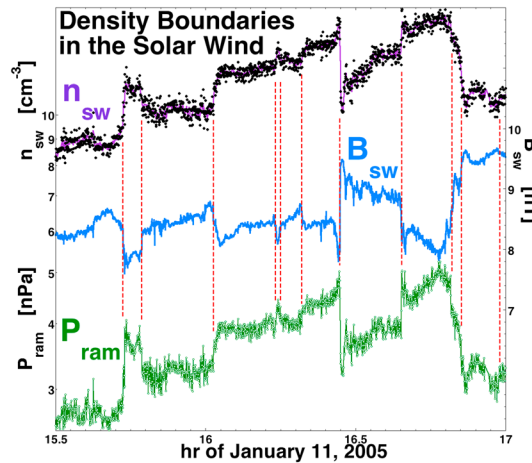
Figure 7. Using Wind 3DP measurements, several proton-density boundaries in the solar wind are denoted by vertical red dashed lines. The purple curve is a 30 s running average of the proton number density n_{sw} (left axis) with the black points being 3 s resolution measurements of n_{sw}. The green curve is the 3 s resolution measurement of the solar wind ram pressure P_{ram} (left axis). The blue curve is the 3 s resolution of the solar wind magnetic field strength B_{sw} (right axis) measured by Wind MAG.

1996] from the years 1995–2005 are used with 1 min time resolution. This data set involves five GOES satellites (GOES 8–GOES 12). For the spacecraft GOES 8, the magnetic field measurements are corrected by subtracting 7.22 nT from the z component magnetic field following the recommendations of *Tsyganenko et al.* [2003]. The GOES magnetic field data are cleaned to eliminate magnetosheath intervals using the methodology of *Borovsky and Denton* [2010a]; this methodology eliminates data when the measured magnetic field is southward, since magnetopause-crossing intervals at geosynchronous orbit are rare when the IMF is northward [*Suvorova et al.*, 2005].

To measure the ram pressure of the solar wind at Earth, proton measurements of the solar wind plasma from the Solar Wind Electron, Proton, and Alpha Monitor (SWEPAM) instrument [*McComas et al.*, 1998] on ACE are used with 64 s time resolution. For a higher-time-resolution look at the ram pressure of the solar wind, 3 s measurements from Wind 3DP [*Lin et al.*, 1995] will be used.

To measure radial flow velocities at geosynchronous orbit in the dayside magnetosphere, cold-ion moments from the multisatellite MPA data set [*Bame et al.*, 1993; *Thomsen et al.*, 1999] from Los Alamos National Laboratory spacecraft are used. The flow measurements from MPA (Magnetospheric Plasma Analyzer) are only utilized if the cold-plasma number density is above $5\,cm^{-3}$.

For the superposed epoch averaging a collection of 70 high-speed-stream-driven storms is used. This list of 70 storms comes from a list of 93 high-speed-stream-driven storms that were used in previous studies [*Denton and Borovsky*, 2012; *Borovsky and Denton*, 2010a, 2010b, 2011], with 23 storms eliminated from the list of 93. The majority of the 23 were eliminated owing to the presence of ejecta in the solar wind during the prestorm and storm intervals, as determined using the new four-plasma solar wind categorization scheme of *Xu and Borovsky* [2015], which identifies ejecta plasma as having an anomalously low proton temperature and/or an anomalously high Alfven speed. A substantial amount of ejecta during a storm interval will change the classification of a storm from a high-speed-stream-driven storm to a hybrid storm. A few of the 23 storms were eliminated owing to the storm being particularly weak or short lived. The zero epoch (trigger) for the superposed averaging is chosen to be the onset of storm levels of magnetospheric convection for each storm event, taken to be the time at which the Midnight Boundary Index (MBI) index crosses the value of 60.7°, which is approximately equivalent to the value of the Kp index being 4+. MBI is an index created from measurements of the location of the low-latitude edge of the diffuse auroral precipitation as determined by DMSP satellite overflights, mathematically shifted to local midnight [*Gussenhoven et al.*, 1983]. The storm onset times were determined to about 30 min accuracy using MBI.

3.2. The Magnetic Field at Geosynchronous Orbit During Storms

In Figure 6 two examples of the global magnetic field strength perturbations of the dayside magnetosphere during high-speed-stream-driven storms are shown. In both plots of Figure 6 the dayside magnetic field strength B_{geo} at geosynchronous orbit as measured by GOES 12 (blue) and GOES 10 (red) are plotted as functions of time when each spacecraft is between 06:00 LT and 18:00 LT. The ram pressure of the solar wind $P_{ram} = m_p n_{sw} v_{sw}^2$ as measured by ACE upstream of the Earth is also plotted (green), delayed by a time $230\,R_E/v_{sw}$. The top plot of Figure 6 is from a high-speed-stream-driven storm in 2004, and the bottom plot is from a high-speed-stream-driven storm in 2005. The local times of the two GOES spacecraft are indicated by the colored numbers next to the GOES curves in Figure 6. When the GOES spacecraft are in the vicinity
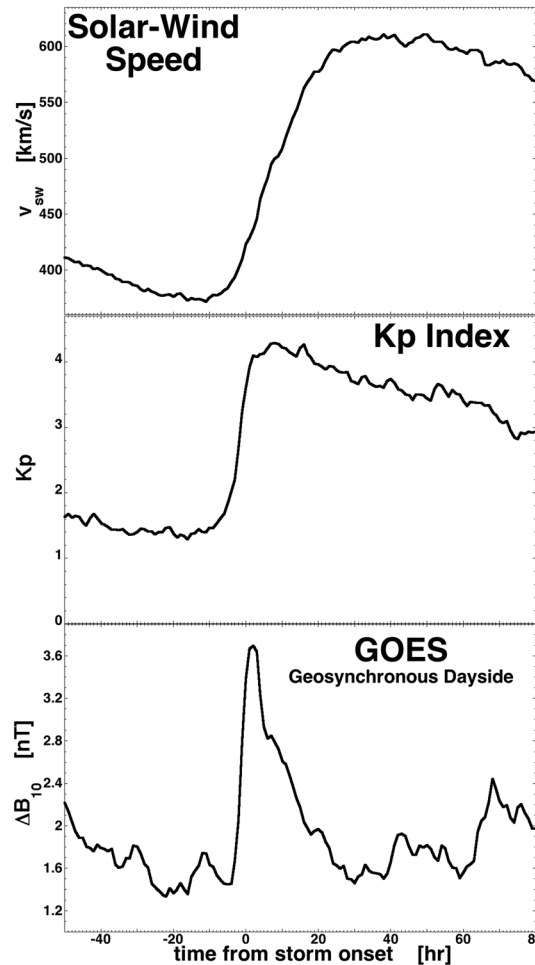
Figure 8. For 70 high-speed-stream-driven geomagnetic storms, superposed epoch averages of the (top) solar wind speed, (middle) Kp index, and (bottom) 10 min change in the geosynchronous magnetic field strength ΔB_{10} are plotted as a function of time with the zero epoch being the onset of the storms. The ΔB_{10} values averaged are from magnetic field measurements by the GOES spacecraft between 09:00 LT and 16:00 LT.

of local noon the response of B_{geo} to P_{ram} can be clearly seen in Figure 6, with both spacecraft (which are separated by 4 h of local time) responding. Near the dawn and dusk regions of geosynchronous orbit the magnetic field strength is not responding as clearly to the solar wind ram pressure, rather the field strength in these regions is determined to a large degree by magnetospheric plasma properties and by magnetospheric currents. Note in Figure 6 the temporal behaviors of B_{geo} that differ on the two spacecraft and that differ from the solar wind ram pressure: on the dayside there can be substantial magnetic field strength perturbations at geosynchronous orbit that are localized and that are not related to upstream solar wind ram-pressure perturbations. Short-time scale localized perturbations could be owed to bow shock kinetic processes such as hot flow anomalies [*Sibeck et al.*, 1999; *Eastwood et al.*, 2008; *Fillingim et al.*, 2011; *Safrankova et al.*, 2012], downstream pressure pulses [*Lin et al.*, 1996; *Archer et al.*, 2012], and foreshock bubbles [*Sibeck et al.*, 2008; *Omidi et al.*, 2010; *Hartinger et al.*, 2013]. The origins of the longer-time scale perturbations that are not associated with the solar wind are not known: they could be caused by plasma diamagnetic effects or by temporally changing magnetospheric currents.

Note in Figure 6 that the ram-pressure changes in the solar wind tend to be sudden. This is because the changes in the ram pressure $m_p n_{\text{sw}} v_{\text{sw}}^2$ tend to be caused by changes in the solar wind density n_{sw} associated with different parcels of plasma and the plasma boundaries in the solar wind are fairly thin. Some examples of this are shown in Figure 7, where several plasma boundaries in the slow solar wind are shown for 90 min of 3 s resolution solar wind measurements by the Wind spacecraft. The plasma boundaries are marked with the red dashed vertical lines; these boundaries are clearly seen in the measurements of the plasma density n_{sw} (black points with purple curve, left axis) by the Wind 3DP instrument and in the measurements of the magnetic field strength B_{sw} (blue curve, right axis) by the Wind MAG instrument [*Lepping et al.*, 1995]. Each of these boundaries has a thickness on the order of 10 s in the spacecraft frame; these plasma boundaries are typically about 4000 km thick, much larger than proton gyroradii (~50 km) and ion inertial lengths (~100 km) in the solar wind. The green curve (left axis) in Figure 7 is the ram pressure of the solar wind P_{ram} measured at 3 s time resolution. As can be seen, sudden jumps in the ram pressure (green curve) are associated with the plasma boundaries and the jumps occur in about 10 s.

The duration of a ram-pressure perturbation is the duration of a plasma parcel (time between plasma boundaries). These plasma-parcel durations have been statistically studied: as can be seen in Figure 3 of *Borovsky* [2012b], there is an abundance of parcels with durations on the order of 10 min.
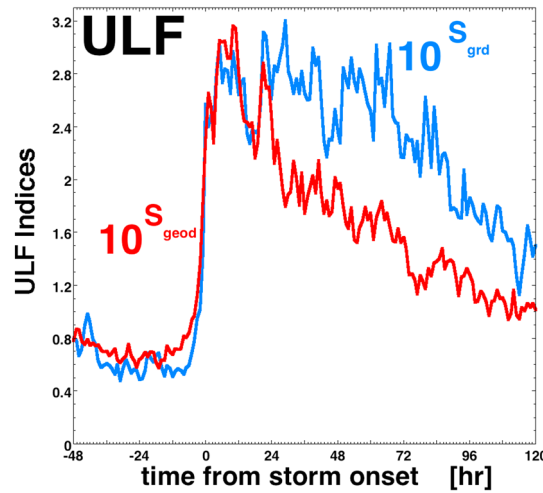
Figure 9. For 70 high-speed-stream-driven geomagnetic storms, superposed epoch averages of the ground-based ULF index S_{grd} (blue) and the geosynchronous ULF index S_{geod} are plotted.

To characterize the compressions of the magnetic field in the dayside magnetosphere at geosynchronous orbit, 10 min changes in the 1 min resolution measurements of the magnetic field strength are examined. This change ΔB_{10} is defined as $\Delta B_{10}(t) = |B_{geo}(t+5\,\text{min}) - B_{geo}(t-5\,\text{min})|$, where B_{geo} is the magnetic field strength $B_{geo} = (B_x^2 + B_y^2 + B_z^2)^{1/2}$.

In Figure 8 the superposed epoch average of ΔB_{10} is plotted for the dayside magnetosphere. In the top plot of Figure 8 the superposed average of the solar wind speed v_{sw} is plotted for the 70 storms, and in the middle plot the Kp index for the 70 storms is plotted. The bottom plot plots ΔB_{10} at geosynchronous orbit.

Measurements of ΔB_{10} that are taken by a GOES spacecraft are only used in Figure 8 when the spacecraft is in the 08:00 LT to 16:00 LT at geosynchronous orbit. Note that the GOES spacecraft are operated in pairs (GOES-east and GOES-west) and that coverage with two GOES spacecraft is sparse when there is a restriction on local time. Hence, superposed epoch averages of the GOES dayside data will be noisy since only 54 of the 70 storms have GOES data coverage. As can be seen in Figure 8, the superposed average of ΔB_{10} is increased substantially during the first day of a high-speed-stream-driven storm and relaxes back to normal values thereafter. Early in the storms the mean values of ΔB_{10} are ~3 nT; later in the storms the mean values of ΔB_{10} are ~2 nT.

The temporal profile of the superposed average of the amplitude ΔB_{10} of the quasi-DC compressive perturbations differs from the temporal profile of the superposed average of the ULF indices, which are measures mainly of noncompressive magnetic fluctuations in the magnetosphere with Fourier periods of 143 s–500 s [Kozyreva et al., 2007; Romanova et al., 2007]. For the 70 high-speed-stream-driven storms, the superposed epoch average of the two ULF indices S_{grd} (blue, measured on the ground) and S_{geod} (red, measured in geosynchronous orbit) are plotted in Figure 9. The "detrended" (subscript "d") ULF indices are used (using the detrending method of Borovsky and Denton [2014]); since the ULF indices S represent the logarithm of the spectral power the quantities 10^S are plotted. As can be seen, both indices rise in magnitude at the onset of storms and both slowly decline in intensity through the several-day-long storms [see also Kozyreva and Kleimenova, 2008]. Note that the decline of the ground-based ULF index S_{grd} is significantly slower than the decline of the geosynchronous-based ULF index S_{geod}: the two indices are different and respond differently to the solar wind [Borovsky and Denton, 2014]. The temporal profiles of the ULF indices (Figure 9) resemble the temporal profiles of the Kp index (Figure 8): indeed, the correlation coefficients between each of the ULF and Kp indices are very high, higher than the correlation coefficients between each other (see Figure 1 and Table 3 of Borovsky and Denton [2014]). These correlation coefficients can be written $r_{corr}(S_{grd},Kp) = +0.74$, $r_{corr}(S_{geod},Kp) = +0.76$, and $r_{corr}(S_{grd},S_{geod}) = +0.66$.

The temporal profile of the superposed average of the amplitude ΔB_{10} of the lower-frequency compressive perturbations also differs from the temporal profile of the superposed average ΔB_1 of higher-frequency compressive perturbations. In Figure 24 of Borovsky and Denton [2010a] the superposed epoch average of the 1 min change ΔB_1 in B_{geo} on the dayside at geosynchronous orbit is plotted. The amplitude of ΔB_1 rises early in the high-speed-stream-driven storms and then persists at elevated values throughout the several-day-long storm periods.

3.3. Radial (Compressional) Flow Velocities at Geosynchronous Orbit

Radial flow velocities can be measured in the dayside magnetosphere at geosynchronous orbit in response to changes in the ram pressure of the solar wind: inward radial flow when the solar wind ram pressure increases and outward radial flow when the solar wind ram pressure decreases. These flow velocities are measured
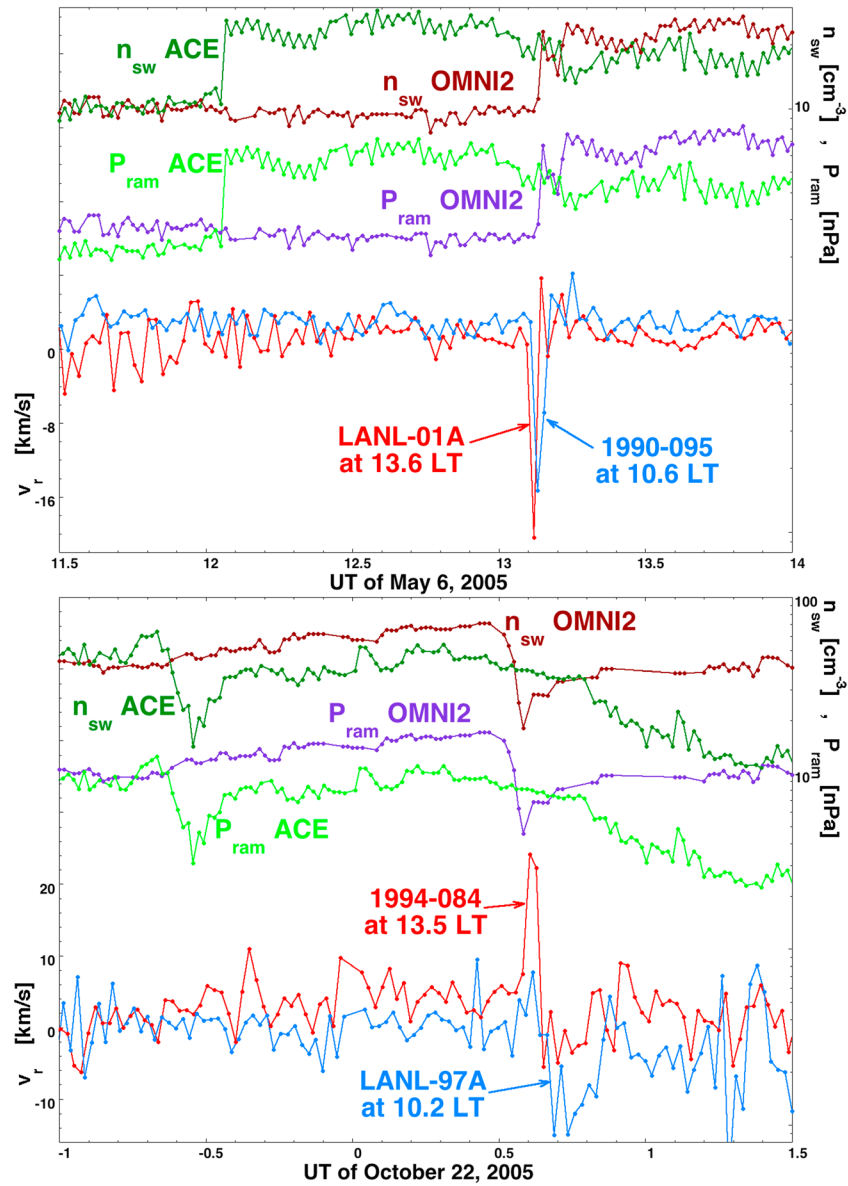
Figure 10. The radial plasma flow velocities v_r as measured by MPA on two spacecraft in geosynchronous orbit are plotted (red and blue) as a function of time (left axis). The solar wind density n_{sw} and ram pressure P_{ram} measured by ACE upstream and advected by OMNI2 are plotted (right axis). (top) A solar wind density increase and (bottom) a solar wind density decrease then increase.

with the MPA instruments but only when there are sufficient amounts of cold plasma present to calculate the flow velocity from the shift of the cold-ion distribution function. The flow measurements can only be made with MPA when a spacecraft is inside the plasmasphere. In the dayside magnetosphere that restricts the flow measurements to quiet geomagnetic conditions when the outer plasmasphere refills to beyond geosynchronous orbit or to plasmaspheric drainage plumes during active times. However, the flow velocities within drainage plumes are temporally irregular [*Borovsky and Denton*, 2008] (owing perhaps to ULF waves during active times or to turbulence in the flow of the plumes), so matching measured flow velocities within plumes to changes in the ram pressure of the solar wind is very difficult.

In the top plot of Figure 10 an isolated ram-pressure change in the solar wind during very quiet geomagnetic conditions is examined at a time when two geosynchronous spacecraft are in the plasmasphere near local noon. The two green curves (right axis) are the number density n_{sw} and ram pressure P_{ram} of the solar wind as measured by the SWEPAM instrument on the ACE spacecraft upstream of the Earth. The dark red and
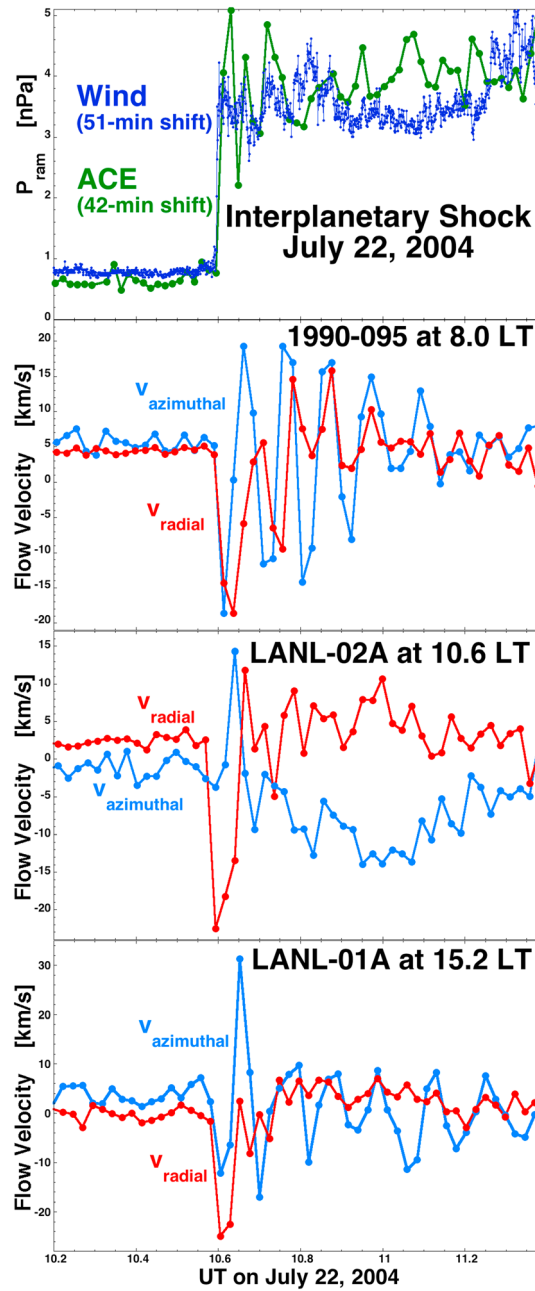
Figure 11. For a forward interplanetary shock hitting the Earth on 22 July 2004, the radial and azimuthal plasma flow velocities at geosynchronous orbit as measured by MPA on three spacecraft are plotted as a function of time. (first panel) The solar wind ram pressure (time shifted to Earth) as measured by ACE (green) and Wind (blue). (second–fourth panels) The plasma flow velocities as measured on the satellites 1990-095, LANL-02A, and LANL-01A, respectively. The second and third panels are prenoon and the fourth panel is postnoon.

purple curves (right axis) are the OMNI2 estimates of the solar wind density n_{sw} and ram pressure P_{ram} at Earth [*King and Papitashvili*, 2005], obtained by advecting the ACE solar wind measurements to the nose of the bow shock. The timing of the pressure change P_{ram} reaching Earth is best obtained from the OMNI2 curves; the temporal profile of the pressure change is best obtained by examining the ACE curves. The red and blue curves (left axis) are measurements of the radial plasma flow velocity obtained by two geosynchronous spacecraft (1990-095 and LANL-01A) carrying the MPA plasma instruments. Both spacecraft are in the high-density plasmasphere this day as they traverse the dayside magnetosphere. When the ram-pressure change reaches Earth at 13:07 UT, the two spacecraft are straddling local noon. In the example of the top plot, inward radial velocities of ~20 km/s are obtained for a ram-pressure increase of ~3.6 nPa. Note that in the 64 s time resolution ACE data of Figure 10 the thickness of the density change and ram-pressure change in the solar wind are not resolved. In Figure 10 the velocity measurements by MPA are also unresolved. The MPA instrument has a time resolution of 86 s and is measuring cold-ion flows during 10.15 s of that 86 s [cf. *Bame et al.*, 1993]: hence, the MPA measurements are snapshots of the cold ions produced once every 86 s.

A second example of radial flows in the magnetosphere associated with ram-pressure changes in the solar wind is examined in the bottom plot of Figure 10. Again, two geosynchronous spacecraft are in the dayside plasmasphere straddling local noon when the ram-pressure perturbation

hits Earth. The temporal profile, a decrease and then increase, of the ram pressure can be seen in the green ACE curves (right axis) at 23:28 UT on 21 October 2005 in the bottom plot. In the dark red and purple curves (right axis) the perturbation is seen to hit the Earth at about 0:35 UT on 22 October 2005. The geosynchronous spacecraft 1994-084 (red curve, left axis) clearly sees an outward (positive) then inward (negative) radial flow associated with the solar wind pressure decrease then increase. The spacecraft LANL-97A (blue curve, left axis)
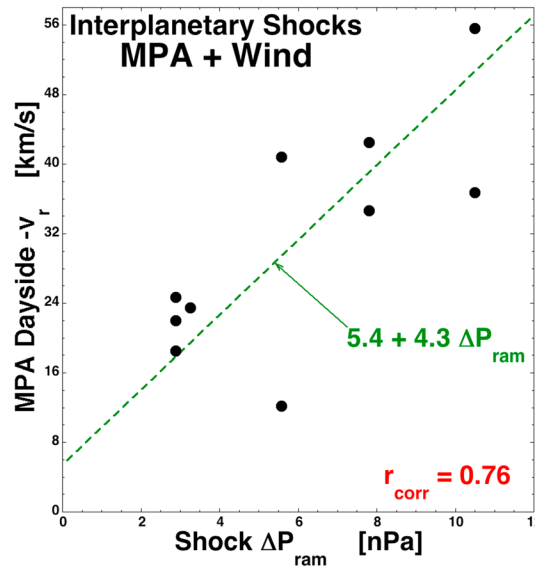
Figure 12. For five forward interplanetary shocks hitting the Earth, the measured radial flow velocities v_r at geosynchronous orbit in the dayside magnetosphere are plotted as a function of the increase in solar wind ram pressure P_{ram} across the shocks. P_{ram} was measured by Wind 3DP and v_r was measured by MPA on multiple spacecraft.

picks up only the inward radial flow. It could be that the outward flow persisted for less than 86 s and the timing of the 10.15 s measurement of cold ions within the 86 s window of MPA was off.

To a limited extent, expression (9) can be applied to the radial velocities measured in the plasmasphere in comparison with $\partial B_{geo}/\partial t$ values. Applying expression (9) is limited by the fact that the spacecraft that carry the MPA detectors do not carry magnetic field instruments, and in general, GOES geosynchronous spacecraft are not proximate to the MPA spacecraft. For the May 2005 event in the top plot of Figure 10 the GOES 12 spacecraft was at 08:00 LT while 1990-095 was at 10.6 LT. GOES 12 saw that $\partial B_{geo}/\partial t =$ +3.35 nT/min = $+5.6 \times 10^{-2}$ nT/s; using this in expression (9) yields $v_r = -5.3$ km/s. This value of v_r is lower than the peak value -15 km/s seen at 10.6 LT, but the measured $\partial B_{geo}/\partial t$ at 08:00 LT was probably weaker than the actual value of $\partial B_{geo}/\partial t$ at 10.6 LT. For the October 2005 event in the bottom plot of Figure 10 the GOES 10 spacecraft was at 15.5 LT while 1994-084 was at 13.5 LT. GOES 10 saw that $\partial B_{geo}/\partial t = -5.9$ nT/min = -9.8×10^{-2} nT/s; using this in expression (9) yields $v_r = +9.3$ km/s. This value 9.3 km/s is smaller than the peak value of 24 km/s measured by MPA, but the measured $\partial B_{geo}/\partial t$ at 15.5 LT was probably less than the actual value of $\partial B_{geo}/\partial t$ at 13.5 LT. The underestimate of v_r by expression (9) may also indicate that the image-dipole model underestimates the displacement of flux surfaces for a given change of the magnetic field strength.

Expression (10) can also be applied to the radial velocities measured in the plasmasphere in comparison with $\partial P_{ram}/\partial t$ values in the solar wind. For the May 2005 event in the top plot of Figure 10 the ACE spacecraft sees a ram-pressure increase of 4.05 nPa in 64 s: this pressure change probably occurred in a time scale less than the 64 s resolution of ACE, but spreading of the pressure profile as it is advected through the magnetosheath probably broadens the time derivative. A change of 4.05 nPa in 64 s is $\partial P_{ram}/\partial t = +6.3 \times 10^{-2}$ nPa/s; using this value in expression (10) yields $v_r = -38$ km/s. The measured peak velocities from the MPA measurements are -20 km/s at 13.6 LT and -15 km/s at 10.6 LT. For the October 2005 event in the bottom plot of Figure 10 the ACE spacecraft sees a decrease of the ram pressure by 9.4 nPa in seven intervals of 64 s. That is $\partial P_{ram}/\partial t = -2.0 \times 10^{-2}$ nPa/s; using this value in expression (10) yields $v_r = +12$ km/s. The measured peak value of the velocity measured by MPA is $+24$ km/s at 13.5 LT, with no flow picked up by MPA at 10.2 LT. The underestimate of v_r by expression (10) may also indicate that the image-dipole model underestimates the displacement of flux surfaces for a given change of the solar wind ram pressure.

In Figure 11 the radial and azimuthal velocities at geosynchronous orbit are examined for a forward interplanetary shock hitting the Earth when three geosynchronous spacecraft are in the plasmasphere in the dayside magnetosphere. In the top plot of Figure 11 the ram pressure P_{ram} of the solar wind is plotted as a function of time as measured by the 3DP plasma instrument on Wind (blue points) and as measured by the SWEPAM instrument on ACE (green curve); the upstream Wind measurements are time shifted by 51 min and the upstream ACE measurements are time shifted by 42 min. The shock is represented here by the sudden temporal increase in P_{ram}. The other three plots of Figure 11 are plots of the flow velocity measured with the MPA instrument on board the three geosynchronous spacecraft within the dayside plasmasphere: 1990-095 was at 08:00 LT when the shock hit, LANL-02A was at 10.6 LT, and LANL-01A was at 15.2 LT. The red curves are the radial velocity (positive being a flow radially away from the Earth and negative being a flow
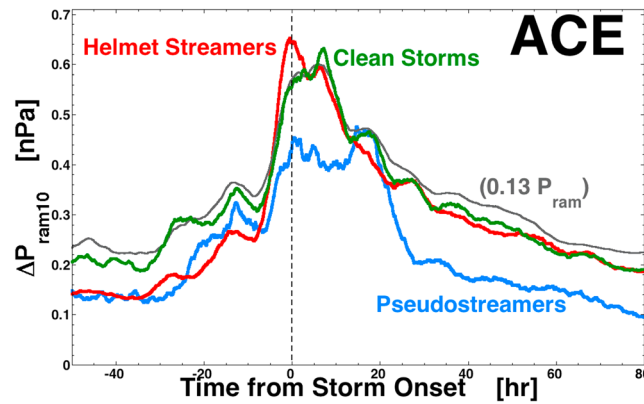
Figure 13. For 29 of the 70 high-speed-stream-driven storms in the collection, the superposed epoch average of the 10 min change ΔP_{ram10} in the solar wind ram pressure P_{ram} is plotted in green. For the same storms 0.13 times the superposed average of P_{ram} is plotted in gray. For a collection of helmet-streamer high-speed stream storms the superposed average of ΔP_{ram10} is plotted in red, and for a collection of pseudostreamer high-speed stream storms the superposed average of ΔP_{ram10} is plotted in blue.

radially toward the Earth), and the blue curves are the azimuthal velocity (positive being eastward in the direction of corotation and negative being westward opposite to the corotation). On all three spacecraft the radial velocities commenced with an inward flow of on the order of 20 km/s. Note the ringing of both the radial and the azimuthal flows in Figure 11: ringing periods ranging from 340 s to 520 s are seen (considerably slower periods than in the low-density magnetosphere of the simulations in Figure 4).

In Figure 12, for five forward interplanetary shocks hitting the Earth when there are MPA instruments in geosynchronous orbit inside the dayside plasmasphere, the inward radial velocities $-v_r$ measured by the MPA instruments are plotted as a function of the ram-pressure change ΔP_{ram} across the interplanetary shocks. The Pearson's linear correlation coefficient r_{corr} between $-v_r$ and ΔP_{ram} is $r_{corr} = +0.76$ for the data of Figure 12. A major-axis linear regression fit [*Pearson*, 1901; *Smith*, 2009] (also known as a "Gaussian fit" [*Borovsky et al.*, 1998] or a "total least squares fit" [*Golub and Van Loan*, 1980]) to the data is plotted as the green dashed line, which is

$$v_r = -4.3 \; \Delta P_{ram} - 5.4, \tag{12}$$

where v_r is in km/s and ΔP_{ram} is in nPa. The value $v_r \sim 20$ km/s for $\Delta P_{ram} \sim 3.6$ nPa obtained in the top plot of Figure 10 approximately fits expression (12).

3.4. Ram-Pressure Fluctuations in the Solar Wind During Storms

To characterize the fluctuations of the ram pressure P_{ram} of the solar wind, 10 min changes in the 64 s resolution measurements of the ram pressure from ACE are calculated. This change ΔP_{ram10} is defined as $\Delta P_{ram10}(t) = |P_{ram}(t + 5 \text{ min}) - P_{ram}(t - 5 \text{ min})|$, where $P_{ram} = m_p n_{sw} v_{sw}^2$. The 70 storms utilized in this study are from the years 1993–2005; 29 of those storms are in the years 1998–2005. In Figure 13 the superposed epoch average of ΔP_{ram10} is plotted in green for the fraction (29 of 70) of the high-speed-stream-driven storms that overlap the years 1998–present of the ACE data set. The superposed average of ΔP_{ram10} becomes very elevated at the onset of the high-speed-stream-driven storms and declines steadily during the first 2 days of the storms. Afterward, ΔP_{ram10} is at typical levels (the mean value of ΔP_{ram10} in the ACE data set is 0.28 nPa). In red and in blue the superposed average of ΔP_{ram10} is plotted for a set of helmet-streamer high-speed stream-driven storms and for a set of pseudostreamer high-speed-stream-driven storms: these two collections of storms are described in *Borovsky and Denton* [2013]. Note in Figure 13 that ΔP_{ram10} tends to be greater in helmet-streamer storms (red) than in pseudostreamer storms (blue). Helmet-streamer storms are preceded by intervals of sector-reversal-region plasma [*Xu and Borovsky*, 2015], which is characterized by strong density fluctuations. The coronal hole plasma of the high-speed stream later in the storms is also on average of lower speed for pseudostreamers than it is for helmet streamers and it has weaker values of ΔP_{ram10}.

The quantity ΔP_{ram10} is strongly correlated with the ram pressure of the solar wind P_{ram}, with a Pearson's linear correlation coefficient $r_{corr} = +0.551$ in the ACE data set. Hence, ΔP_{ram10} tends to be large when P_{ram} is large. In Figure 13 the superposed average of P_{ram} is plotted in gray, multiplied by 0.13 to approximately match the amplitude of ΔP_{ram10}. As can be seen by comparing the green and gray curves, the temporal profiles of ΔP_{ram10} and P_{ram} are very similar in the storm time superposed averages.

For the two years, 2004 and 2005, Figure 14 ΔP_{ram10} is plotted as a function of $\Delta n_{sw10} = |n_{sw}(t + 5 \text{ min}) - n_{sw}(t - 5 \text{ min})|$ in the top plot and as a function of $\Delta v_{sw10} = |v_{sw}(t + 5 \text{ min}) - v_{sw}(t - 5 \text{ min})|$ in the bottom plot.
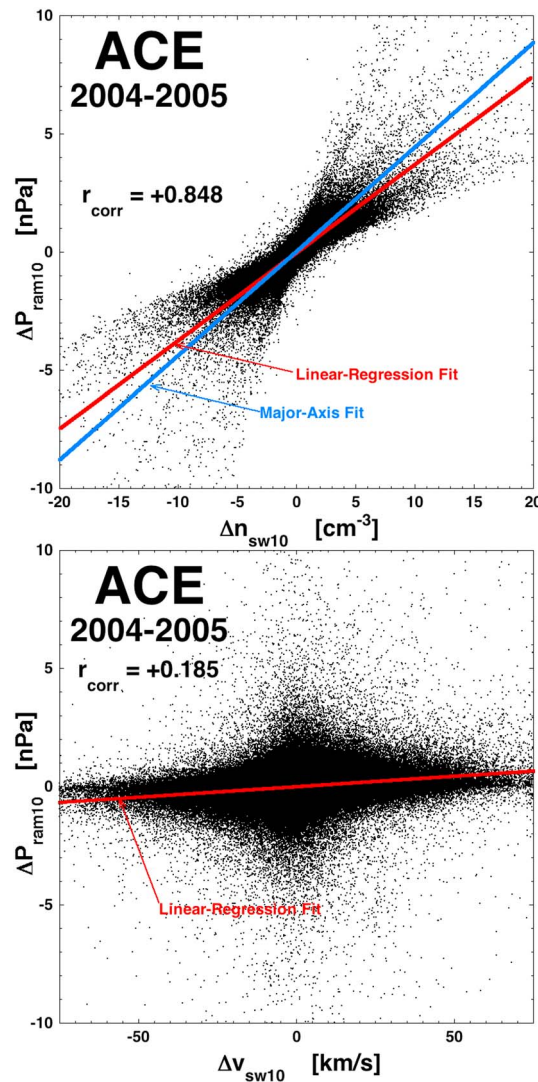
Linear regression fits are plotted in red in both plots, and a major-axis linear regression fit is plotted in blue in the top plot. The Pearson's linear correlation coefficients are noted in each plot. ΔP_{ram10} is highly correlated with Δn_{sw10} with a Pearson's linear correlation coefficient $r_{corr} = +0.848$ in the ACE data set. On the contrary, ΔP_{ram10} is only weakly correlated with Δv_{sw10} with $r_{corr} = +0.185$. Hence, changes in the solar wind ram pressure are dominantly associated with changes in the solar wind number density and much more weakly associated with changes in the solar wind speed.

4. Amplitude Statistics of the Magnetic Field Compressions, the Ram-Pressure Changes, and the Radial Flow Velocities

In Figure 15 the magnitudes of the change ΔB in the magnetic field strength B_{geo} of the dayside magnetosphere are explored for time intervals δt different from 10 min. Using the GOES magnetic field data set for 1998–2005 restricted to local times from 11:00 LT to 13:00 LT, the mean value of $\Delta B_{\delta t}$ taken at a time interval δt defined as $\Delta B_{\delta t}(t) = |B_{geo}(t+\delta t) - B_{geo}(t-\delta t)|$ is plotted as a function of δt. In Figure 15 the $\Delta B_{\delta t}$ values are normalized to ΔB_{10}. As seen in the plot, $\Delta B_{\delta t}$ increases for values of δt that are larger than 10 min but not

Figure 14. For the 64 s resolution ACE measurements in 2004 and 2005, the 10 min change ΔP_{ram10} in the solar wind ram pressure is plotted (top) as a function of the 10 min change in the solar wind number density and (b) as a function of the 10 min change in the solar wind speed.

by much. $\Delta B_{\delta t}$ decreases strongly as $\delta t \rightarrow 1$ min. The ratio $\Delta B_{\delta t}/\Delta B_{10}$ as a function of δt is well fit by the logarithmic function $0.33 + 0.69[\log_{10}(\delta t)]^{3/2}$ that is plotted as the red dashed curve in Figure 15, which is valid for $1\,min \leq \delta t \leq 30\,min$. The curve $0.33 + 0.69[\log_{10}(\delta t)]^{3/2}$ also fits the normalized change $\Delta B_{\delta t}/B_{mag}$ in comparison with $\Delta B_{10}/B_{mag}$.

In Figure 16 the size distributions of ΔB_{10} values, ΔP_{ram10} values, and $|v_r|$ values are examined. In the top plot the occurrence distribution of ΔB_{10} values in the 1998–2005 GOES geosynchronous magnetic field data set for local times between 11:00 LT and 13:00 LT is plotted in black. Variable size binning was used for the various ranges of ΔB_{10} values, so the units of the distribution function are arbitrary. The red dashed curve plotted in the top plot of Figure 16 is a $\Delta B_{10}{}^{-3}$ power law. As can be seen by the approximate agreement between the plotted points and the red dashed curve, larger values of ΔB_{10} in the dayside magnetosphere approximately obey power law statistics. The largest values of ΔB_{10} in the top plot can be identified with interplanetary shocks reaching the Earth.

In the middle plot of Figure 16 the occurrence distribution of ΔP_{ram10} in the solar wind is plotted. The ΔP_{ram10} distribution was obtained from ACE SWEPAM 64 s measurements of the solar wind in the years 2003 and

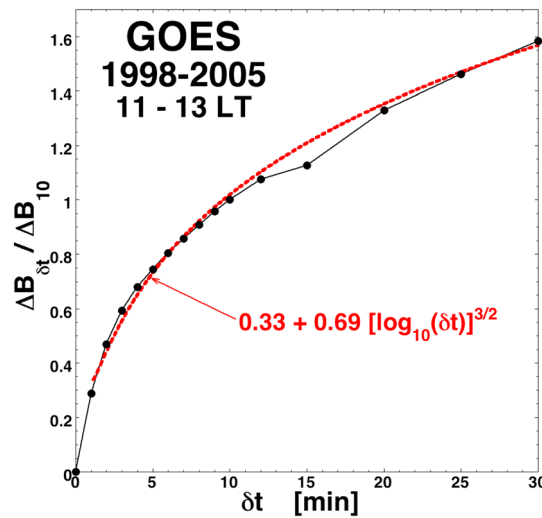**Figure 15.** Calculating the change $\Delta B_{\delta t}$ in the geosynchronous magnetic field strength near local noon over a time scale δt, the ratio of $\Delta B_{\delta t}$ to the 10 min change ΔB_{10} is plotted as a function of δt. The values used are the mean values for the multisatellite GOES data set in the years 1998–2005.

2004. The red dashed curve in the second plot is a $\Delta P_{ram10}{}^{-3}$ power law. As was the case for the ΔB_{10} values in the dayside magnetosphere in the top plot, the occurrence distribution of ΔP_{ram10} values in the solar wind approximately obeys power law statistics for large values. Note that the two power laws that fit the large values of ΔB_{10} and of ΔP_{ram10} both have exponents -3. Most of the largest values of ΔP_{ram10} in the middle plot are identified with interplanetary shocks; a few are identified with sudden density changes in the solar wind.

In the bottom plot of Figure 16 the occurrence distribution of radial velocities at geosynchronous orbit in the dayside magnetosphere is plotted. T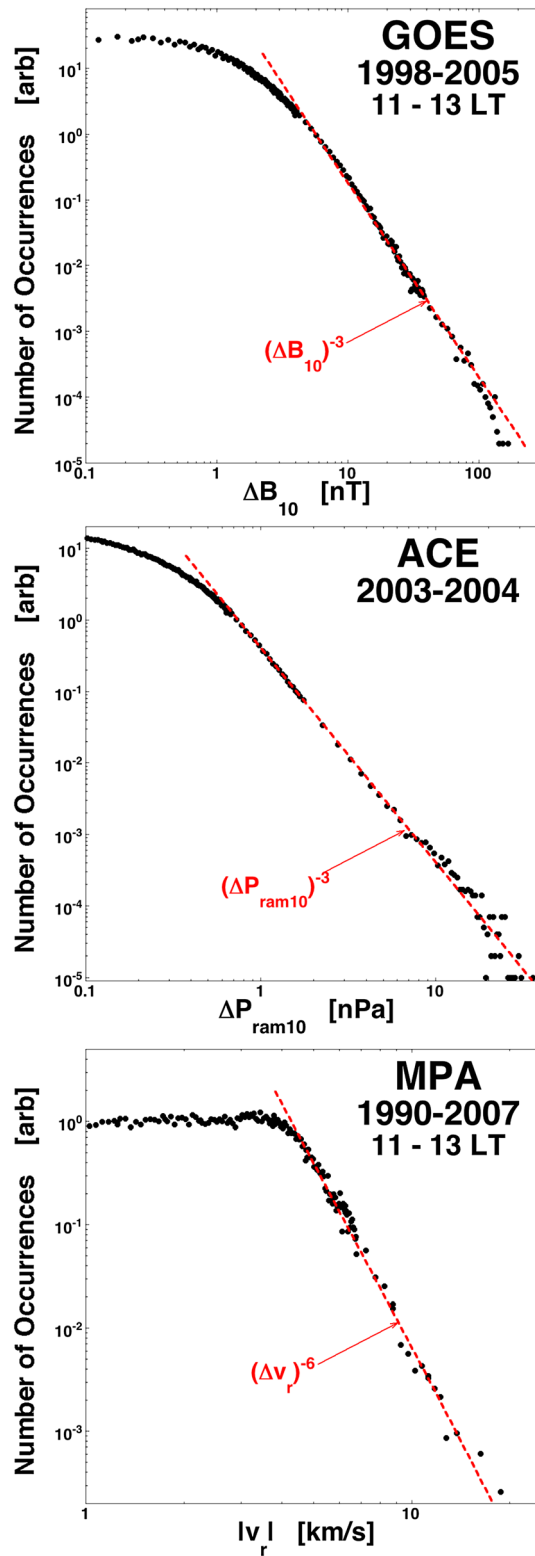he $|v_r|$ values were obtained from multisatellite MPA measurements at geosynchronous orbit in the local time range between 11:00 LT and 13:00 LT in the years 1990 to 2007. The $|v_r|$ values used to construct the distribution function in the bottom plot came from times when the MPA spacecraft were in the filled plasmasphere during intervals of low Kp. The red dashed curve in the bottom plot of Figure 16 is a $|v_r|^{-6}$ power law. As were the cases for the distributions of ΔB_{10} and ΔP_{ram10} values in the top two plots of Figure 16, for large values the radial flow velocities $|v_r|$ in the dayside magnetosphere approximately obey power law statistics. Note that the approximate power law indices of ΔB_{10} and ΔP_{ram10} are similar, but the index for $|v_r|$ differs significantly. The reason why the distribution of velocities $|v_r|$ has a different form from the distribution of pressure changes is not known. One possibility is that the flow velocity associated with ΔP_{ram10} has a duration that is considerably less than 10 min. For example, if the velocity only lasted 1 min then a single large value of ΔP_{ram10} would be associated with nine small values of velocity and one large value of velocity. There would be fractionally less values of high velocity than of high ΔP_{ram10}; hence, the high-velocity tail of the distribution would be weaker than that of ΔP_{ram10}.

5. Summary

For magnetic pumping calculations, the quasi-DC compressions of the Earth's dayside magnetic field by density fluctuations in the solar wind have been characterized. Magnetic field measurements at geosynchronous orbit, plasma flow measurements at geosynchronous orbit, and global MHD simulations were used in conjunction with solar wind plasma measurements.

As the field strength in the dayside magnetosphere changes, there is a radial displacement of flux surfaces and a radial advection of plasma. Calculating the radial displacement of flux surfaces in an image-dipole model, it is predicted that the magnetic compression of parcels of plasma in the dayside magnetosphere is bigger than the change in magnetic field strength observed on board a spacecraft. The image-dipole model predicts that plasma compression can be a factor of 2 higher than the measured magnetic field compression. This plasma-compression prediction is not confirmed with spacecraft measurements owing to the radial motion of the plasma parcels as they are compressed; however, tests of the predicted radial velocity for the image-dipole model find that the model underpredicts the plasma radial velocities and hence probably underpredicts the amount of plasma compression.

Examination of the solar wind demonstrated that the ram-pressure changes causing the quasi-DC magnetospheric compressions are mostly owed to changes in the solar wind number density being advected past the Earth. Rapid changes in the solar wind number density associated with the crossing of plasma boundaries

Figure 16. The occurrence distributions are plotted for (top) the 10 min change ΔB_{10} in the dayside magnetic field strength at geosynchronous orbit, (middle) the 10 min change ΔP_{ram10} of the solar wind ram pressure, and (bottom) the radial flow velocity v_r in the dayside magnetosphere at geosynchronous orbit. In all three plots the red dashed curve is a power law.

produce rapid changes in the solar wind ram pressure; an Earth crossing of a plasma boundary produces a sudden change in the dayside magnetic field strength accompanied by a sudden inward or outward motion of the plasma in the dayside magnetosphere.

Superposed epoch analysis triggered on the temporal onsets of high-speed stream-driven storms was used to explore solar wind compressions and geosynchronous magnetic field compressions during high-speed stream-driven storms, which are of particular interest for the energization of the outer electron radiation belt. Mean values of the 10 min change ΔB_{10} of the geosynchronous dayside field strength are $\Delta B_{10} \sim 3$ nT early in storms and are $\Delta B_{10} \sim 2$ nT later in storms.

The occurrence distributions of (a) 10 min changes in the geosynchronous dayside magnetic field strength ΔB_{10}, (b) 10 min changes in the solar wind ram pressure ΔP_{ram10}, and (c) instantaneous geosynchronous dayside radial flow velocities $|v_r|$ were examined. All three distributions approximately obey power law statistics for large values. In particular, the approximate power law indices for the distributions of ΔB_{10} and ΔP_{ram10} values are both -3. The power law index for the $|v_r|$ distribution is closer to -6.

6. Discussion: Nightside Compressions

This report characterized the temporal compressions of the dayside magnetosphere at geosynchronous orbit. On the dayside of the relative magnitude of the compressions $\Delta B_{mag10}/B_{mag}$ are a few percent to tens of percent and the plasma motions associated with the dayside compressions are discernible radial displacements inward or outward as the magnetic field strength B_{mag} increases or decreases.
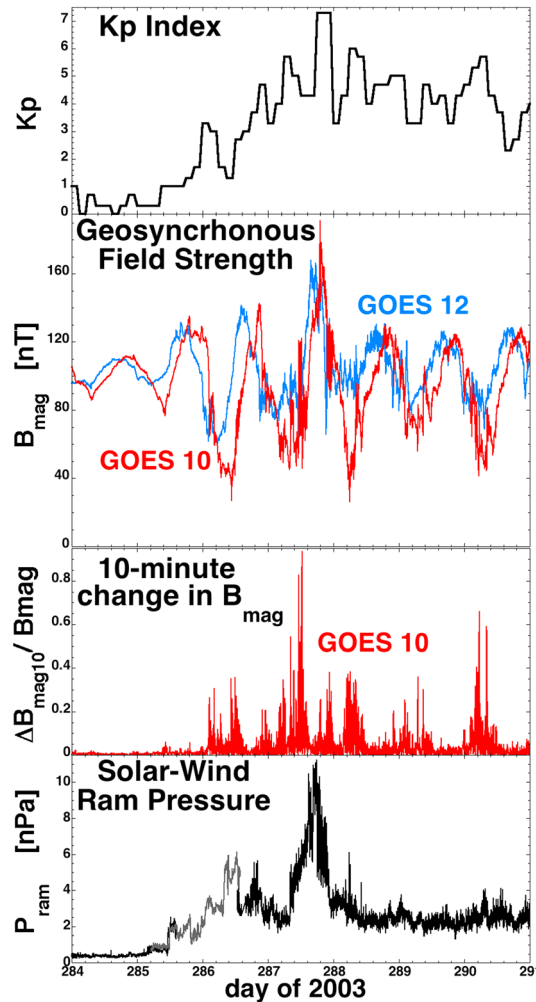
Figure 17. For 7 days in 2003 where geomagnetic activity goes from quiet to a high-speed-stream-driven storm, the magnetic field strength at geosynchronous orbit is examined. (first panel) The Kp index is plotted as a function of time, (second panel) the magnetic field strengths as measured by GOES 10 (red) and GOES 12 (blue) are plotted, (third panel) the 10 min change in the geosynchronous field strength measured by GOES 10 is plotted, and (fourth panel) the solar wind ram pressure as measured by ACE (black) and Wind (gray) is plotted.

Temporal compressions of the nightside magnetosphere are not so easily characterized from the spacecraft data. In Figure 17 the magnetic field strength B_{mag} measured by two GOES spacecraft in geosynchronous orbit is plotted for 7 days as a high-speed-stream-driven geomagnetic storm commences. The Kp index is plotted in the top plot. Day 284 is at the end of a "calm before the storm" with the storm commencing toward the end of day 285. The storm is ongoing from day 286 to beyond the end of the plot. The second panel of Figure 17 plots the measured magnetic field strength B_{mag}, with GOES 10 plotted in red and GOES 12 plotted in blue. The local maximum of B_{mag} once a day occurs when each spacecraft is on the dayside, and the local minimum of B_{mag} that occurs each day occurs when each spacecraft is on the nightside. In the third panel of Figure 17 the 10 min change ΔB_{mag10} in the magnetic field strength, normalized to the magnetic field strength B_{mag}, is plotted for GOES 10. The localized peaks in $\Delta B_{mag10}/B_{mag}$ occur when GOES 10 is on the nightside. Note that these nightside values of $\Delta B_{mag10}/B_{mag}$ approach unity. In the fourth panel of Figure 17 the solar wind ram pressure P_{ram} is plotted as a function of time. Comparing the second and fourth panels one can see that the changes in the magnitude of the magnetic field are related to the

solar wind ram pressure when the GOES spacecraft is on the dayside, but such a relationship is not clear when the GOES spacecraft is on the nightside.

The magnetic field strength changes at geosynchronous orbit in the nightside magnetosphere may be caused by temporally changing magnetospheric currents, or by moving magnetospheric currents, or by plasma diamagnetism, or by other causes. In the nightside magnetosphere at geosynchronous orbit the plasma motions associated with the temporal changes in the magnetic field strength, and hence the plasma compressions, would be difficult to characterize and quantify.

References

Alfven, H. (1950), On the origin of cosmic radiation. II, *Phys. Rev.*, *77*, 375, doi:10.1103/PhysRev.77.375.

Alfven, H. (1959), Momentum spectrum of the Van Allen radiation, *Phys. Rev. Lett.*, *3*, 459, doi:10.1103/PhysRevLett.3.459.

Alfven, H., and C.-G. Falthammar (1963), *Cosmical Electrodynamics*, Oxford Univ. Press, New York.

Archer, M. O., T. S. Horbury, and J. P. Eastwood (2012), Magnetosheath pressure pulses: Generation downstream of the bow shock from solar wind discontinuities, *J. Geophys. Res.*, *117*, A05228, doi:10.1029/2011JA017468.

Bame, S. J., D. J. McComas, M. F. Thomsen, B. L. Barraclough, R. C. Elphic, J. P. Glore, J. T. Gosling, J. C. Chavez, E. P. Evans, and F. J. Wymer (1993), Magnetospheric plasma analyzer for spacecraft with constrained resources, *Rev. Sci. Instrum.*, *64*, 1026, doi:10.1063/1.1144173.

Berger, J. M., W. A. Newcomb, J. M. Dawson, E. A. Friedman, R. M. Kulsrud, and A. Lenard (1958), Heating of a confined plasma by oscillating electromagnetic fields, *Phys. Fluids*, *1*, 301, doi:10.1063/1.1705888.

Berube, D., J. Sanny, R. Taus, and A. Garoutte (2014), Dayside distribution of Pc5 wave power in the quiet magnetosphere and its response to the solar wind, *Planet. Space Sci.*, *97*, 1, doi:10.1016/j.pss.2014.04.012.

Borodkova, N. L., J.-B. Liu, Z.-H. Huang, G. N. Zastenker, C. Wang, and P. E. Eiges (2006), Effect of change in large and fast solar wind dynamic pressure on geosynchronous magnetic field, *Chin. Phys.*, *15*, 2458, doi:10.1088/1009-1963/15/10/045.

Borodkova, N. L., J. B. Liu, Z. H. Huang, and G. N. Zastenker (2008), Geosynchronous magnetic field response to the large and fast solar wind dynamic pressure changes, *Adv. Space Res.*, *41*, 1220, doi:10.1016/j.asr.2007.05.075.

Borovsky, J. E. (1986), Magnetic pumping by magnetosonic waves in the presence of noncompressive electromagnetic fluctuations, *Phys. Fluids*, *29*, 3245, doi:10.1063/1.865842.

Borovsky, J. E. (2012a), The effect of sudden wind shear on the Earth's magnetosphere: Statistics of wind-shear events and CCMC simulations of magnetotail disconnections, *J. Geophys. Res.*, *117*, A06224, doi:10.1029/2012JA017623.

Borovsky, J. E. (2012b), Looking for evidence of mixing in the solar wind from 0.31 to 0.98 AU, *J. Geophys. Res.*, *117*, A06107, doi:10.1029/2012JA017525.

Borovsky, J. E., and M. H. Denton (2008), A statistical look at plasmaspheric drainage plumes, *J. Geophys. Res.*, *113*, A09221, doi:10.1029/2007JA012994.

Borovsky, J. E., and M. H. Denton (2010a), Magnetic field at geosynchronous orbit during high-speed stream-driven storms: Connections to the solar wind, the plasma sheet, and the outer electron radiation belt, *J. Geophys. Res.*, *115*, A08217, doi:10.1029/2009JA015116.

Borovsky, J. E., and M. H. Denton (2010b), On the heating of the outer radiation belt to produce high fluxes of relativistic electrons: Measured heating rates for high-speed stream-driven storms, *J. Geophys. Res.*, *115*, A12206, doi:10.1029/2010JA015342.

Borovsky, J. E., and M. H. Denton (2011), A survey of the anisotropy of the outer electron radiation belt during high-speed-stream-driven storms, *J. Geophys. Res.*, *116*, A05201, doi:10.1029/2010JA016151.

Borovsky, J. E., and M. H. Denton (2013), The differences between storms driven by helmet-streamer CIRs and storms driven by pseudo-streamer CIRs, *J. Geophys. Res. Space Physics*, *118*, 5506–5521, doi:10.1002/jgra.50524.

Borovsky, J. E., and M. H. Denton (2014), Exploring the cross correlations and autocorrelations of the ULF indices and incorporating the ULF indices into the systems science of the solar wind-driven magnetosphere, *J. Geophys. Res. Space Physics*, *119*, 4307–4334, doi:10.1002/2014JA019876.

Borovsky, J. E., and P. J. Hansen (1991), The breaking of the first adiabatic invariants of particles in time-dependent magnetic fields: Computer simulations and theory, *Phys. Rev. A*, *43*, 5605, doi:10.1103/PhysRevA.43.5605.

Borovsky, J. E., C. K. Goertz, and G. Joyce (1981), Magnetic pumping of particles in the outer Jovian magnetosphere, *J. Geophys. Res.*, *86*, 3481–3495, doi:10.1029/JA086iA05p03481.

Borovsky, J. E., M. F. Thomsen, and R. C. Elphic (1998), The driving of the plasma sheet by the solar wind, *J. Geophys. Res.*, *103*, 17,617–17,639, doi:10.1029/97JA02986.

Borovsky, J. E., B. Lavraud, and M. M. Kuznetsova (2009), Polar cap potential saturation, dayside reconnection, and changes to the magnetosphere, *J. Geophys. Res.*, *114*, A03224, doi:10.1029/2009JA014058.

Borovsky, J. E., M. H. Denton, R. E. Denton, V. K. Jordanova, and J. Krall (2013), Estimating the effects of ionospheric plasma on solar-wind/magnetosphere coupling via mass loading of dayside reconnection: Ion-plasma-sheet oxygen, plasmaspheric drainage plumes, and the plasma cloak, *J. Geophys. Res. Space Physics*, *118*, 5695–5719, doi:10.1002/jgra.50527.

Borovsky, J. E., R. H. W. Friedel, and M. H. Denton (2014), Statistically measuring the amount of pitch-angle scattering that energetic electrons undergo as they drift across the plasmaspheric drainage plume at geosynchronous orbit, *J. Geophys. Res. Space Physics*, *119*, 1814–1826, doi:10.1002/2013JA019310.

Chan, K.-W., and R. E. Holzer (1976), ELF hiss associated with plasma density enhancements in the outer magnetosphere, *J. Geophys. Res.*, *81*, 2267–2274, doi:10.1029/JA081i013p02267.

Chappell, C. R., M. M. Huddleston, T. E. Moore, B. L. Giles, and D. C. Delcourt (2008), Observations of the warm plasma cloak and an explanation of its formation in the magnetosphere, *J. Geophys. Res.*, *113*, A09206, doi:10.1029/2007JA012945.

Chen, F. F. (1974), *Introduction to Plasma Physics*, Sect. 9.4, Plenum Press, New York.

Claudepierre, S. G., S. R. Elkington, and M. Wiltberger (2008), Solar wind driving of magnetospheric ULF waves: Pulsations driven by velocity shear at the magnetopause, *J. Geophys. Res.*, *113*, A05218, doi:10.1029/2007JA012890.

Denton, M. H., and J. E. Borovsky (2012), Magnetosphere response to high-speed solar wind streams: A comparison of weak and strong driving and the importance of extended periods of fast solar wind, *J. Geophys. Res.*, *117*, A00L05, doi:10.1029/2011JA017124.

Dmitriev, A. V., M. F. Bakhareva, and Y. S. Minaeva (2001), Electron acceleration by magnetic pumping on the tail magnetopause, *Adv. Space Res.*, *28*, 807, doi:10.1016/S0273-1177(01)00528-2.

Dunham, W. D., S. A. MacIntyre, and C. R. Upton (1996), Design and performance of the GOES-8 high resolution magnetometer, *SPIE Proc.*, *2812*, 365.

Eastwood, J. P., et al. (2008), THEMIS observations of a hot flow anomaly: Solar wind, magnetosheath, and ground-based measurements, *Geophys. Res. Lett.*, *35*, L17S03, doi:10.1029/2008GL033475.

Eastwood, J. P., S. J. Schwartz, T. S. Horbury, C. M. Carr, K.-H. Glassmeier, I. Richter, C. Koenders, F. Plaschke, and J. A. Wild (2011), Transient Pc3 wave activity generated by a hot flow anomaly: Cluster, Rosetta, and ground-based observations, *J. Geophys. Res.*, *116*, A08224, doi:10.1029/2011JA016467.

Eriksson, P. T. I., A. D. M. Walker, and J. A. E. Stephenson (2006), A statistical correlation of Pc5 pulsations and solar wind pressure oscillations, *Adv. Space Res.*, *38*, 1763, doi:10.1016/j.asr.2005.08.023.

Fillingim, M. O., J. P. Eastwood, G. K. Parks, V. Angelopoulos, I. R. Mann, S. B. Mende, and A. T. Weatherwax (2011), Polar UVI and THEMIS GMAG observations of the ionospheric response to a hot flow anomaly, *J. Atmos. Sol. Terr. Phys.*, *73*, 137, doi:10.1016/j.jastp.2010.03.001.

Friedel, R. H. W., G. D. Reeves, and T. Obara (2002), Relativistic electron dynamics in the inner magnetosphere—A review, *J. Atmos. Sol. Terr. Phys.*, *64*, 265, doi:10.1016/S1364-6826(01)00088-8.

Glauert, S. A., and R. B. Horne (2005), Calculation of pitch angle and energy diffusion coefficients with the PADIE code, *J. Geophys. Res.*, *110*, A04206, doi:10.1029/2004JA010851.

Goertz, C. K. (1978), Energization of particles in Jupiter's outer magnetosphere, *J. Geophys. Res.*, *83*, 3145–3150, doi:10.1029/JA083iA07p03145.

Golub, G. H., and C. F. Van Loan (1980), An analysis of the total least squares problem, *SIAM J. Numer. Anal.*, *17*, 883, doi:10.1137/0717073.

Gussenhoven, M. S., D. A. Hardy, and N. Heinemann (1983), Systematics of the equatorward diffuse auroral boundary, *J. Geophys. Res.*, *88*, 5692–5708, doi:10.1029/JA088iA07p05692.

Hartinger, M. D., D. L. Turner, F. Plaschke, V. Angelopoulos, and H. Singer (2013), The role of transient ion foreshock phenomena in driving Pc5 ULF wave activity, *J. Geophys. Res. Space Physics*, *118*, 299–312, doi:10.1029/2012JA018349.

Hayakawa, M., N. Ohmi, M. Parrot, and F. Lefeuvre (1986), Direction finding of ELF hiss emissions in a detached plasma region of the magnetosphere, *J. Geophys. Res.*, *91*, 135–141, doi:10.1029/JA091iA01p00135.

Hughes, W. J., D. J. Southwood, B. Mauk, R. L. McPherron, and J. N. Barfield (1978), Alfven waves generated by an inverted plasma energy distribution, *Nature*, *275*, 43, doi:10.1038/275043a0.

Jordanova, V. K., Y. S. Miyoshi, S. Zaharia, M. F. Thomsen, G. D. Reeves, D. S. Evans, C. G. Mouikis, and J. F. Fennell (2006), Kinetic simulations of ring current evolution during the Geospace Environment Modeling challenge events, *J. Geophys. Res.*, *111*, A11S10, doi:10.1029/2006JA011644.

Kepko, L., and H. E. Spence (2003), Observations of discrete, global magnetospheric oscillations directly driven by solar wind density variations, *J. Geophys. Res.*, *108*(A6), 1257, doi:10.1029/2002JA009676.

Kepko, L., H. E. Spence, and H. J. Singer (2002), ULF waves in the solar wind as direct drivers of magnetospheric pulsations, *Geophys. Res. Lett.*, *29*(8), 1197, doi:10.1029/2001GL014405.

Kessel, R. L. (2008), Solar wind excitation of Pc5 fluctuations in the magnetosphere and on the ground, *J. Geophys. Res.*, *113*, A04202, doi:10.1029/2007JA012255.

King, J. H., and N. E. Papitashvili (2005), Solar wind spatial scales in and comparisons of hourly Wind and ACE plasma and magnetic field data, *J. Geophys. Res.*, *110*, A02104, doi:10.1029/2004JA010649.

Kivelson, M. G., and D. J. Southwood (1985), Resonant ULF waves: A new interpretation, *Geophys. Res. Lett.*, *12*, 49–52, doi:10.1029/GL012i001p00049.

Kovalevskiy, I. V. (1980), Ion-cyclotron instability in the frontal boundary layer of the geomagnetosphere produced by detached plasma clouds, *Geomagn. Aeron.*, *20*, 338.

Kovalevskiy, I. V. (1981), Cyclotron instability during interaction of detached plasma regions with the plasma sheet during substorms, *Geomagn. Aeron.*, *21*, 83.

Kozyreva, O., V. Pilipenko, M. J. Engebretson, K. Yumoto, J. Watermann, and N. Romanova (2007), In search of a new ULF wave index: Comparison of Pc5 power with dynamics of geostationary relativistic electrons, *Planet. Space Sci.*, *55*, 755, doi:10.1016/j.pss.2006.03.013.

Kozyreva, O. V., and N. G. Kleimenova (2008), Estimation of storm-time level of day-side wave geomagnetic activity using a new ULF index, *Geomagn. Aeron.*, *48*, 491, doi:10.1134/S0016793208040099.

Lepping, R. P., et al. (1995), The Wind magnetic field investigation, *Space Sci. Rev.*, *71*, 207, doi:10.1007/BF00751330.

Li, L. Y., J. B. Cao, J. Y. Yang, and Y. X. Dong (2013), Joint response of geosynchronous magnetic field and relativistic electrons to external changes in solar wind dynamic pressure and interplanetary magnetic field, *J. Geophys. Res. Space Physics*, *118*, 1472–1482, doi:10.1002/jgra.50201.

Lin, R. P., et al. (1995), A three-dimensional plasma and energetic particle investigation for the Wind spacecraft, *Space Sci. Rev.*, *71*, 125, doi:10.1007/BF00751328.

Lin, Y., L. C. Lee, and M. Yan (1996), Generation of dynamic pressure pulses downstream of the bow shock by variations in the interplanetary magnetic field orientation, *J. Geophys. Res.*, *101*, 479–493, doi:10.1029/95JA02985.

Liu, W. W., and G. Rostoker (1995), Energetic ring current particles generated by recurring substorm cycles, *J. Geophys. Res.*, *100*, 21,897–21,910, doi:10.1029/95JA01934.

Liu, W. W., G. Rostoker, and D. N. Baker (1999), Internal acceleration of relativistic electrons by large-amplitude ULF pulsations, *J. Geophys. Res.*, *104*, 17,391–17,407, doi:10.1029/1999JA900168.

Lyon, J. G., J. A. Fedder, and C. M. Mobarry (2004), The Lyon-Fedder-Mobarry (LFM) global MHD magnetospheric simulation code, *J. Atmos. Sol. Terr. Phys.*, *66*, 1333, doi:10.1016/j.jastp.2004.03.020.

Mann, I. R., A. N. Wright, K. J. Mills, and V. M. Nakariakov (1999), Excitation of magnetospheric waveguide modes by magnetosheath flows, *J. Geophys. Res.*, *104*, 333–353, doi:10.1029/1998JA900026.

Mathie, R. A., and I. R. Mann (2000), A correlation between extended intervals of ULF wave power and storm-time geosynchronous relativistic electron flux enhancements, *Geophys. Res. Lett.*, *27*, 3261–3264, doi:10.1029/2000GL003822.

Mathie, R. A., and I. R. Mann (2001), On the solar wind control of Pc5 ULF pulsation power at mid-latitudes: Implications for MeV electron acceleration in the outer radiation belt, *J. Geophys. Res.*, *106*, 29,783–29,796, doi:10.1029/2001JA000002.

McComas, D. J., et al. (1998), An unusual coronal mass ejection: First Solar Wind Electron, Proton, Alpha Monitor (SWEPAM) results from the Advanced Composition Explorer, *Geophys. Res. Lett.*, *25*, 4289–4292, doi:10.1029/1998GL900174.

Menk, F. W., T. K. Yeoman, D. M. Wright, M. Lester, and F. Honary (2003), High-latitude observations of impulse-driven ULF pulsations in the ionosphere and on the ground, *Ann. Geophys.*, *21*, 559, doi:10.5194/angeo-21-559-2003.

Merkin, V. G., and J. G. Lyon (2010), Effects of the low-latitude ionospheric boundary condition on the global magnetosphere, *J. Geophys. Res.*, *115*, A10202, doi:10.1029/2010JA015461.

Motoba, T., S. Fujita, T. Kikuchi, and T. Tanaka (2007), Solar wind dynamic pressure forced oscillation of the magnetosphere-ionosphere coupling system: A numerical simulation of directly pressure-forced geomagnetic pulsations, *J. Geophys. Res.*, *112*, A11204, doi:10.1029/2006JA012193.

Mu, J.-L. (1993), A new magnetic pumping accelerator of charged particles in Jupiter's magnetosphere, *Geophys. Res. Lett.*, *20*, 1463–1466, doi:10.1029/93GL01595.

Murty, G. S., and R. K. Varma (1958), Acceleration of cosmic radiation, *Phys. Rev.*, *112*, 1789, doi:10.1103/PhysRev.112.1789.

Nakamura, R., J. B. Blake, S. R. Elkington, D. N. Baker, W. Baumjohann, and B. Klecker (2002), Relationship between ULF waves and radiation belt electrons during the March 10, 1998, storm, *Adv. Space Res.*, *30*, 2163, doi:10.1016/S0273-1177(02)80210-1.

Olson, P., and H. Amit (2006), Changes in the Earth's dipole, *Naturwissenschaften*, *93*, 519, doi:10.1007/s00114-006-0138-6.

Omidi, N., J. P. Eastwood, and D. G. Sibeck (2010), Foreshock bubbles and their global magnetospheric impacts, *J. Geophys. Res.*, *115*, A06204, doi:10.1029/2009JA014828.

Ozeke, L. G., and I. R. Mann (2008), Energization of radiation belt electrons by ring current ion driven ULF waves, *J. Geophys. Res.*, *113*, A02201, doi:10.1029/2007JA012468.

Pearson, K. (1901), On lines and planes of closest fit to systems of points in space, *Philos. Mag.*, *2*, 559, doi:10.1080/14786440109462720.

Rastatter, L., M. M. Kuznetsova, D. G. Sibeck, and D. H. Berrios (2012), Scientific visualization to study flux transfer events at the Community Coordinated Modeling Center, *Adv. Space Res.*, *49*, 1623, doi:10.1016/j.asr.2011.12.034.

Regi, M., M. De Lauetis, P. Francia, and U. Villante (2014), The propagation of ULF waves from the Earth's foreshock region to ground: The case study of 15 February 2009, *Earth Planets Sci.*, *66*, 43.

Romanova, N., and V. Pilipenko (2009), ULF wave indices to characterize the solar wind-magnetosphere interaction and relativistic electron dynamics, *Acta Geophys.*, *57*, 158, doi:10.2478/s11600-008-0064-4.

Romanova, N., V. Plipenko, N. Crosby, and O. Khabarova (2007), ULF wave index and its possible applications in space physics, *Bulg. J. Phys.*, *34*, 136.

Rostoker, G., S. Skone, and D. N. Baker (1998), On the origin of relativistic electrons in the magnetosphere associate with some geomagnetic storms, *Geophys. Res. Lett.*, *25*, 3701–3704, doi:10.1029/98GL02801.

Safrankova, J., O. Goncharov, Z. Nemecek, L. Prech, and D. G. Sibeck (2012), Asymmetric magnetosphere deformation driven by hot flow anomaly(ies), *Geophys. Res. Lett.*, *39*, L15107, doi:10.1029/2012GL052636.

Schield, M. A. (1969), Pressure balance between solar wind and magnetosphere, *J. Geophys. Res.*, *74*, 1275–1286, doi:10.1029/JA074i005p01275.

Schluter, A. (1957), Der gyro-relaxations-effect, *Z. Naturforsch.*, *12a*, 822.

Shprits, Y. Y., N. P. Meredith, and R. M. Thorne (2007), Parameterization of radiation belt electron loss timescales due to interactions with chorus waves, *Geophys. Res. Lett.*, *34*, L11110, doi:10.1029/2006GL029050.

Sibeck, D. G., et al. (1999), Comprehensive study of the magnetospheric response to a hot flow anomaly, *J. Geophys. Res.*, *104*, 4577–4593, doi:10.1029/1998JA900021.

Sibeck, D. G., N. Omidi, I. Dandouras, and E. Lucek (2008), On the edge of the foreshock: Model-data comparisons, *Ann. Geophys.*, *26*, 1539, doi:10.5194/angeo-26-1539-2008.

Singer, H. J., C. T. Russell, M. G. Kivelson, E. W. Greenstadt, and J. V. Olsen (1977), Evidence for the control of Pc 3,4 magnetic pulsations by the solar-wind velocity, *Geophys. Res. Lett.*, *4*, 377–379, doi:10.1029/GL004i009p00377.

Singer, H. J., L. Matheson, R. Grubb, A. Newman, and S. D. Bouwer (1996), Monitoring space weather with the GOES magnetometers, *SPIE Proc.*, *2812*, 299.

Smith, R. J. (2009), Use and misuse of the reduced major axis for line-fitting, *Am. J. Phys. Antrop.*, *140*, 476, doi:10.1002/ajpa.21090.

Spasojevic, M., and S. A. Fuselier (2009), Temporal evolution of proton precipitation associated with the plasmaspheric plume, *J. Geophys. Res.*, *114*, A12201, doi:10.1029/2009JA014530.

Spitzer, L., and L. Witten (1953), On the ionization and heating of a plasma, *USAEC Rep. NYO-999*, March.

Summers, D., B. Ni, N. P. Meredith, R. B. Horne, R. M. Thorne, M. B. Moldwin, and R. R. Anderson (2008), Electron scattering by whistler-mode ELF hiss in plasmaspheric plumes, *J. Geophys. Res.*, *113*, A04219, doi:10.1029/2007JA012678.

Suvorova, A., A. Dmitriev, J.-K. Chao, M. Thomsen, and Y.-H. Yang (2005), Necessary conditions for geosynchronous magnetopause crossings, *J. Geophys. Res.*, *110*, A01206, doi:10.1029/2003JA010079.

Takahashi, K., and A. Y. Ukhorskiy (2008), Timing analysis of the relationship between solar wind parameters and geosynchronous Pc5 amplitude, *J. Geophys. Res.*, *113*, A12204, doi:10.1029/2008JA013327.

Thomsen, M. F., E. Noveroske, J. E. Borovsky, and D. J. McComas (1999), Calculating the moments from measurements by the Los Alamos magnetospheric plasma analyzer, LA-13566-MS, Los Alamos Natl. Lab.

Thorne, R. M., T. P. O'Brien, Y. Y. Shprits, D. Summers, and R. B. Horne (2005), Timescale for MeV electron microburst loss during geomagnetic storms, *J. Geophys. Res.*, *110*, A09202, doi:10.1029/2004JA010882.

Thorne, R. M., R. B. Horne, V. K. Jordanova, J. Bortnik, and S. Glauert (2006), Interaction of EMIC waves with thermal plasma and radiation belt particles, in *Magnetospheric ULF Waves*, edited by K. Takahashi et al., pp. 213 , AGU, Washington, D. C.

Tsyganenko, N. A., H. J. Singer, and J. C. Kasper (2003), Storm-time distortion of the inner magnetosphere: How severe can it get?, *J. Geophys. Res.*, *108*(A5), 1209, doi:10.1029/2002JA009808.

Viall, N. M., L. Kepko, and H. E. Spence (2009), Relative occurrence rates and connection of discrete frequency oscillations in the solar wind density and dayside magnetosphere, *J. Geophys. Res.*, *114*, A01201, doi:10.1029/2008JA013334.

Walker, A. D. M. (1998), Excitation of magnetohydrodynamic cavities in the magnetosphere, *J. Atmos. Sol. Terr. Phys.*, *60*, 1279, doi:10.1016/S1364-6826(98)00077-7.

Wang, C., J. B. Liu, Z. H. Huang, and J. D. Richardson (2007), Response of the magnetic field at the geosynchronous orbit to solar wind dynamic pressure pulses, *J. Geophys. Res.*, *112*, A12210, doi:10.1029/2007JA012664.

Wing, S., and D. G. Sibeck (1997), Effects of interplanetary magnetic field z component and the solar wind dynamic pressure on the geosynchronous magnetic field, *J. Geophys. Res.*, *102*, 7207–7216, doi:10.1029/97JA00150.

Xu, F., and J. E. Borovsky (2015), A new 4-plasma categorization scheme for the solar wind, *J. Geophys. Res. Space Physics*, *120*, 70–100, doi:10.1002/2014JA020412.